



RIVAS
SCP0-GA-2010-265754



RIVAS
Railway Induced Vibration Abatement Solutions
Collaborative project

**Ground vibration from turnouts: numerical and experimental tests for
identification of the main influencing sources/factors**

Deliverable D3.12

Submission date: 31/12/2013

Project Coordinator:
Wolfgang Behr
International Union of Railways (UIC)
ext.behr@uic.org

Title	Ground vibration from turnouts: numerical and experimental tests for identification of the main influencing sources/factors
Domain	WP 3.3
Date	31.12.2013
Author/Authors	Roger Müller, Baldrik Faure, Estelle Bongini, Armin Zemp, Jens Nielsen, Björn Pålsson,
Partner	SBB, SNCF, EMPA, Chalmers University of Technology
Document Code	RIVAS_SBB_WP3_D3_12_V05
Version	5
Status	Final

Dissemination level:

Project co-funded by the European Commission within the Seventh Framework Programme		
Dissemination Level		
PU	Public	X
PP	Restricted to other programme participants (including the Commission Services)	
RE	Restricted to a group specified by the consortium (including the Commission) Services)	
CO	Confidential, only for members of the consortium (including the Commission Services)	

Document history		
Revision	Date	Description
	23/09/2013	Skeleton report
1	29/10/2013	First draft report
2	26/11/2013	Second draft report
3	29/11/2013	Third draft
4	04/12/2013	Final draft
5	31/12/2013	Final

1. EXECUTIVE SUMMARY

Within the frame of the EU FP7 project 'Railway Induced Vibration Abatement Solutions (RIVAS)', abatement measures for ground-borne noise and vibrations for tracks at grade are studied. Workpackage 3.3 of RIVAS focuses on railway infrastructure based vibration reduction technologies for curves and turnouts.

Following the results presented in the deliverable 3.6 [1] in which installation of soft USP in turnout has proved to be non-relevant, it has been decided among the RIVAS WP3 T3 partners to study the issue of ground vibration due to turnouts in an upstream point of view.

First, a measurement campaign carried out in France allows proposing a relevant measurement device as well as an adapted analysis methodology for the turnout characterization in terms of ground borne vibration generation. Results for this particular turnout illustrate the type of analysis that could be used for mitigation measures design. The results particularly show that different phenomena occur all along the turnout: some parts of the turnout could be considered as specific sources of vibrations and noise whereas other could be considered as normal straight track with specific dynamic behaviour.

These results also confirm what is generally highlighted in the literature: impact load at the nose of the turnout due to the wheel transition between the nose and the wing rail of the turnout and variation of global stiffness along the turnout that causes an increase on the wheel-rail interaction force are among the two main sources for noise and ground vibration generation in a turnout.

Therefore, the following chapters of this deliverable present investigations that have been carried out to quantify the effect of modifications in a turnout that could have an impact on these two main sources:

- A large campaign carried out by SBB based on axlebox acceleration measurement when the test train was passing on various turnouts allows checking the effect of USP installation on the wheel-rail interaction force as well as the effect of different turnout designs on this contact force. Soft USP installation does not seem to have an effect on the interaction force. This result has to be handled with care since the comparison is made for two turnouts with the same design but not exactly at the same site.
- In parallel, a process to numerically design ground vibration mitigation measure for turnout, developed by Chalmers University, is used to optimize the geometric parameters of the nose of the turnout in order to minimize the wheel-rail impact load and hence the induced ground vibration. It is demonstrated that the high constraints on the crossing panel geometry, due to the limited allowable dimensions of the transition zone, make this optimization not effective. It is therefore recommended in order to minimize the impact load to soften the crossing panel by using soft railpads.

2. TABLE OF CONTENTS

1. Executive Summary	3
2. Table of contents	4
3. Introduction	5
4. Identification of generation phenomena in a turnout in terms of ground vibration and noise	6
4.1 Description of the site and of the experimental set-up	6
4.2 Track characteristics	9
4.3 Indicators at pass-by	10
4.4 Noise measurements	11
4.5 Ground vibration measurements	14
4.6 Conclusions	16
5. Assessment of wheel-rail interaction in turnouts based on axlebox measurements ...	19
5.1 Axlebox measurements	19
5.2 Analysis of measurements	20
5.2.1 Investigated test sites	21
5.2.2 Spatial resolution	23
5.2.3 Measurement data for Rubigen test site	24
5.2.4 Measurement data for Wichtrach test site	28
5.2.5 Integral quantities for the comparison of different turnout designs	32
5.2.6 Effect of under sleeper pad on acceleration levels	34
5.2.7 Effect of turnout radius on lateral acceleration levels	34
5.3 Conclusions	36
6. Numerical simulation for optimizing the geometry of crossing nose, in terms of groundborne vibration generation	37
6.1 Crossing geometry	37
6.2 Rail profile parameterisation	40
6.3 Optimisation procedure	42
6.4 Optimisation of longitudinal profiles	43
6.5 Conclusions	48
7. Conclusions	50
8. Literature	51

3. INTRODUCTION

Within the frame of the EU FP7 project 'Railway Induced Vibration Abatement Solutions (RIVAS)', abatement measures for ground-borne noise and vibrations for tracks at grade are studied. Workpackage 3.3 of RIVAS focuses on railway infrastructure based vibration reduction technologies for curves and turnouts¹.

In the first step for the development of mitigation measures dedicated to turnouts, an empirical approach was done by installing hard under sleeper pads ($c_{\text{stat}} = 0.22 \text{ N/mm}^3$) in a turnout. The consecutive measurement campaign for cost effective mitigation measure characterization, presented in Deliverable D3.6 [1], came out with unclear and non-consistent results: it seems that no relevant mitigation effects can be achieved.

Following these results, it has been decided among the RIVAS WP3 Task 3 partners to study the issue of ground vibration due to turnout from a "basic principle" point of view.

First, a measurement campaign has been carried out in France to identify and characterize the different types of source that cause noise and ground vibrations along a turnout. The presentation of this measurement campaign also gives relevant identification of the methodology to be used to characterize any turnout, in terms of ground vibration generation.

Second, on-board measurements of axle-box acceleration when a train passes over various turnouts are presented. These results allow for studying the effect of turnout design and USP installation in a turnout on the wheel-rail interaction force.

Finally, as the impact load on the crossing nose is identified as a major source for ground vibration generation from a turnout, a numerical simulation is used to optimize crossing panel geometry to reduce this impact load.

¹ The word "crossing" here is used only for the crossing nose part of a turnout. The word "switch" is used just for the switch part of a turnout. The word turnout is including all parts (switch panel, crossing panel etc.).

4. IDENTIFICATION OF GENERATION PHENOMENA IN A TURNOUT IN TERMS OF GROUND VIBRATION AND NOISE

The following study allows to propose a methodology for characterizing a turnout in terms of ground borne vibration and noise generation; relying on relevant measurement devices and an adapted post-processing analysis, the different sources of noise and vibration are identified, and phenomena at work are characterized.

The work presented here is part of the SNCF project “Noise from Singular Points” started in 2010 and initiated by SNCF Innovation & Research. In this project, specific noise sources are assessed in terms of radiated noise: rail joints, steel bridges and turnouts.

In the first part of the project, an inventory of these sources has been taken in the region of Paris. These sources have been classified depending on the acoustic performance of the track they belong to. Almost half of the counted turnouts were found to be located in tracks with bad acoustic performances [2]. In those areas (mostly with high density of population), annoyance due to ground vibration is also pointed out. Therefore, this specific source of railway noise and vibration represents a major issue for the acceptability of railway transportation in inhabited areas.

In a railway network, turnouts and crossings are key components: they guarantee flexibility and modularity through high technological features. As a consequence, they require costly maintenance operations in order to keep their level of functionality and security. For these reasons, turnouts have been widely investigated for maintenance purposes, as for example in the European project Innotrack [3] or in some work supported by Chalmers Railway Mechanics [4]. Indeed, the phenomena at work in turnouts are numerous and complex and classical theories do not apply in this case. As a result, SNCF Innovation & Research decided to carry out an experimental study in order to identify and characterize the different vibro-acoustic sources in a turnout.

4.1 DESCRIPTION OF THE SITE AND OF THE EXPERIMENTAL SET-UP

The results presented here can also be found in the SNCF paper [2]. For this study, it was decided to focus on a simple case. A single turnout is considered for which all trains are taking the main route in a single direction (trailing move: from the crossing panel towards the switch panel), and only vertical excitations are accounted for. The traffic is mixed: High Speed Trains (TGV), Regional Trains (Diesel Railcars, EMU), Passenger Rail Cars (Corail) and Freight trains.

The turnout (see Figure 4.1 and 4.2) is located in the north-east of France near the town of Saint-Hilaire-au-Temple (Champagne region). The tangent at crossing is 0.085 (1:12) with a radius of around 600 m. For these traffic conditions, the following potential sources have been identified on the turnout:

- Transition between bi-bloc concrete sleepers (regular track) and wooden sleepers (turnout),
- Transition between 60E1 (UIC60), 50E6 (U50) and 46E2 (U33) rails and associated welds,

- Welds in homogeneous track sections,
- Isolated joints,
- Crossing nose,
- Wheel/rail transition from switch rail to stock rail.

In this report we focus on the crossing nose and on the switch blade. The tests consisted in track characterization measurements and in noise and ground vibration measurements at train pass-by. The tests were all performed along the turnout for the two different sources mentioned above and also for a reference section passed by the same trains.

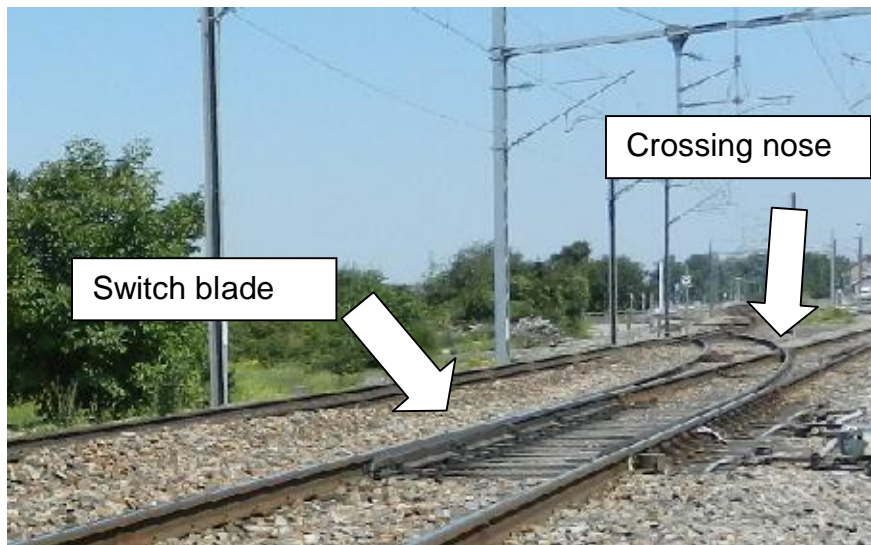


Figure 4.1: General view of the turnout.



Figure 4.2: Track view of the reference section (left) and of the turnout (right). Trains are coming from the back to the front, crossing the reference section at first.

The track in the reference section is built with bi-bloc concrete sleepers ($M = 160$ kg), 46E2 rail (also known as U33 with $M_l = 46.27$ kg/m) and standard rubber rail pads (thickness 4.5 mm). The turnout section is built with wooden sleepers and different types of rail and different fastening systems:

- Along the crossing zone, double length wooden sleepers are used, with 50E6 rails ($M_l = 50.9$ kg/m) and standard rail pads (thickness 9 mm).

- Along the switch panel, regular wooden sleepers are used, with 60E1 rails ($M_l = 60$ kg/m) and turnout specific fastening systems, most likely with standard rubber pads (thickness 9 mm).

The measurements performed on the turnout are summarized in Figure 4.3. Acoustic measurements at pass-by (blue bullets) were performed on both sides of the turnout: on the component side (i.e. on the track side facing the crossing nose and the switch panel) and on the opposite side. The microphones with a distance of 7.5 m to the centre of the track have a position of 1.2 m above track level, the microphones with a distance of 25 m to the centre of the track have a position of 3.5 m above track level.

Ground vibration measurements at pass-by (red squares) were performed only on one side of the turnout, in distance of 8 m and 32 m to the track. Measurements performed in a distance of 16 m could not be evaluated due to technical problems with the sensors.

In order to study impact loads effects, the low frequency track receptance was measured at the following points:

- At the crossing, right after the gap between the nose and the wing rail (where impact is expected).
- At the location where the wheel/rail contact jumps from the switch blade to the stock rail (two measurements, one under each).

In order to study the track dynamics related to rolling noise, the high frequency track receptance at mid-span was measured for the crossing zone and for the switch panel, on the rail opposite to the component (see Figure 4.3). This intends to be representative of the track behaviour along the crossing zone and along the switch panel, both seen as homogeneous sections for which rolling noise theory could be applied.

Track receptance measurements were performed using impact hammer excitation with adapted weight and material for the head of the hammer: heavy hammer and plastic head for low frequencies, light hammer and steel head for high frequencies.



Figure 4.3: Description of the measured quantities. Ground vibration (■) and noise (●) measurements at pass-by. Low frequency (x, x, x) and high frequency (+, +) track receptance.

All the measurements previously mentioned for the turnout were also performed at the reference section:

- low frequency track receptance,
- high frequency track receptance at mid-span,
- ground vibration at pass-by at 8 m and 32 m to the track,
- noise levels at pass-by at 7.5 m and 25 m to the track.

The train type and speed is known for each train.

4.2 TRACK CHARACTERISTICS

The track receptance is given in Figure 4.4 for low frequencies (left) and for high frequencies (right).

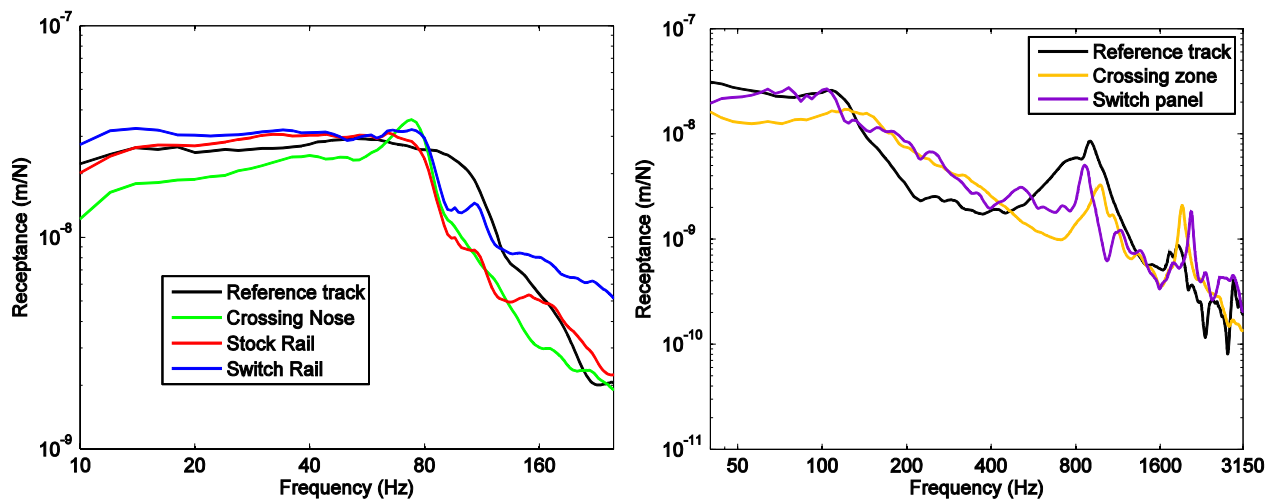


Figure 4.4: Low frequency track receptance under sources (left). High frequency track receptance at mid-span for homogeneous sections (right).

At the very left side of Figure 4.4 (left), we can roughly see the static behaviour of the track at the given locations. It is related to the track ability to generate, transmit or attenuate impact loads or moving loads excitations (quasi static excitation). The major conclusions are:

- The track is stiff under the crossing nose, even if wooden sleepers are used. This might be due to the fact that this track component is larger than a rail, with probably less bending. High impact loads will be generated at the crossing.
- There is a difference between the stiffness of the switch rail and the stiffness of the stock rail. While passing over, the wheel-rail-contacts change from on to the other rail so that the wheels will experience that change of stiffness. This might generate some kind of impact.

With increasing frequencies ($f > 80$ Hz, see figure 4.4 left), the track stiffness is more related to the track response under the dynamic excitations coming from the Wheel/Track interactions (unevenness excitation, parametric excitation). The major conclusions are:

- There is a resonance of the crossing on the ballast stiffness at around 80 Hz. This will lead to a resonance of the dynamic excitation generated at the crossing.
- The track under the crossing is stiff compared to the reference track, except at the 80 Hz resonance. Energy will be transmitted to the ground.

- Below 80 Hz, a softening of the track is observed under the switch panel region compared to the reference track (blue and red curves compared to black curve in Figure 4.4, left). It is more accentuated under the switch rail than under the stock rail. After the ballast cut-off frequency, a softening of the track is once again observed under the switch panel (above 120 Hz for the switch rail and above 160 Hz for the stock rail).
- For the rail opposite to the nose and the switch blade, a softer track compared to the reference track is also observed above 120/160 Hz (purple and orange curves compared to black curve in Figure 4.4, right). In the frequency regions where the track is softer under the turnout than for the reference track, we can expect a mitigation of ground vibration due to non-impulsive excitation phenomena.

The high frequency track dynamics, more related to rolling noise, is given in Figure 4.4 (right). For the reference track, the sharp resonance peak at the pinned-pinned frequency² is almost mixed up with the rail on pad resonance, which is broader (around 800 Hz). The pads are very stiff in this case (around 750 kN/mm). For the crossing zone and the switch panel, the pinned-pinned resonance is less pronounced (the track properties are not really varying periodically along a turnout), and the rail on pads resonance is almost not visible. Therefore there is a large frequency band between 120 Hz and 400 Hz, where the reference track is stiffer than the track at the crossing section and at the switch panel. Vibration waves will be trapped in the rail along the turnout instead of being dissipated as it is the case for the reference track. This could lead to an increase of the noise radiated by the rail or the sleepers which are the main sources for rolling noise in this frequency range [5].

4.3 INDICATORS AT PASS-BY

The time of analysis $T_p = t_2 - t_1$ (pass-by duration) is defined as the time between the first axle is in front of any sensor at the crossing nose (#2 or #3) and the last axle is in front of the same sensor, plus 3 m at each extremity (see Figure 4.5).

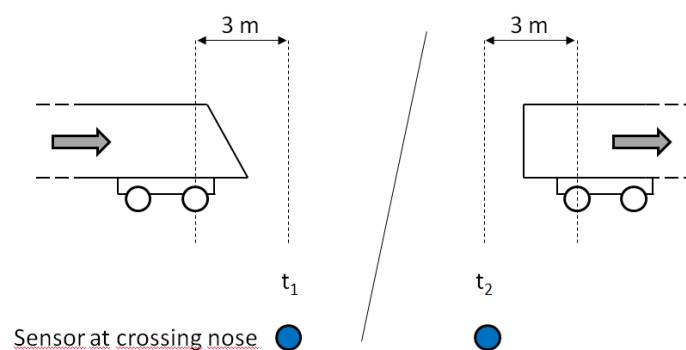


Figure 4.5: Definition of the pass-by duration $T_p = t_2 - t_1$.

The data measured at pass-by are analysed in terms of extra level $\Delta_L = L_{eq, T_p}^{Swi} - L_{eq, T_p}^{Ref}$ and power spectral density. The extra level is defined in Eq. (4.1).

² Frequency at which the wavelength of the vertical bending waves in the rail is equal to twice the sleeper spacing.

$$\Delta_L = L_{eq, T_p}^{Swi} - L_{eq, T_p}^{Ref} \quad (4.1)$$

Where:

L_{eq, T_p}^{Swi} is the equivalent level (of noise or Ground vibration) at pass-by for the switch (turn-out) site, integrated over the pass-by time T_p^{swi} .

L_{eq, T_p}^{Ref} is the equivalent level (of noise or ground vibration) at pass-by for the reference site, integrated over the pass-by time T_p^{ref} .

If the train speed is different between the turnout site and the reference site, the corresponding pass-by durations are different. However, trains with a speed difference of more than 10 % between the two sites are not processed.

For a given measured signal $s(t)$, the equivalent level at pass-by is given by Eq. (4.2) and (4.3):

$$L_{eq, T_p} = 20 \log_{10} \left(\frac{P_{RMS}(s)}{P_0} \right) \quad (4.2)$$

$$P_{RMS}(s) = \sqrt{\frac{1}{T_p} \int_{t_1}^{t_2} s^2(t) dt} \quad (4.3)$$

Where P_0 is a reference value that depends on the nature of the signal $s(t)$. For acoustic measurements $P_0 = 20 \cdot 10^{-6}$ Pa and for an acceleration signal $P_0 = 1 \cdot 10^{-6}$ ms⁻².

The Power Spectral Densities (PSD) at pass-by are estimated using the Welch's method. The signal $s(t)$ is divided in N_b blocs of N_s samples such as $N_s / F_e = 1$ s, where F_e is the sampling frequency. The overlapping ratio between two blocs is 50%. For each bloc k , the discrete Fourier transform $S_k(f)$ is computed over the N_s samples using a Hanning window. The PSD in decibels is finally estimated by averaging the PSDs over the N_b blocs.

$$\hat{S}(f)_{dB} = 20 \log_{10} \left(\frac{1}{N_b} \sum_{k=1}^{N_b} S_k(f) \cdot S_k^*(f) \right) - 20 \log_{10}(P_0) \quad (4.4)$$

If the pass-by duration $T_p < 1.5$ s, only one block of length T_p is considered.

4.4 NOISE MEASUREMENTS

In this section, we focus on the noise radiation in terms of extra noise level $\Delta_L = L_{eq, T_p}^{Swi} - L_{eq, T_p}^{Ref}$ (see Eq. (4.1)) plotted versus the equivalent level L_{eq, T_p}^{Ref} at the reference section. The extra noise levels are given in Figure 4.6 for the microphones at 7.5 m and in Figure 4.7 for the microphones at 25 m.

Figure 4.6 and Figure 4.7 show that a noise increase is observed all around the turnout. This extra noise is more important for silent trains (left part of the x-axis) than for noisy trains (right part of the x-axis).

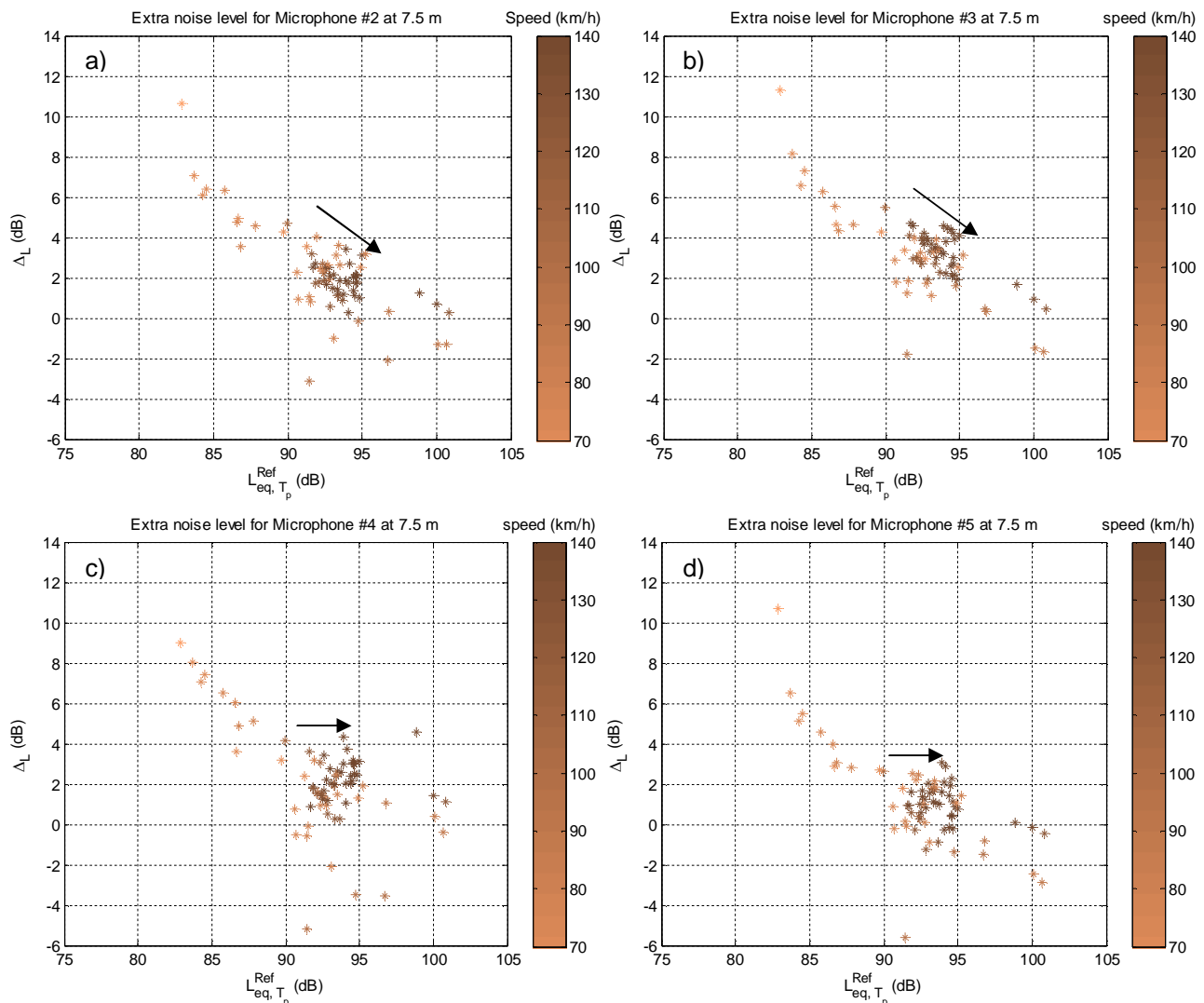


Figure 4.6: Extra noise levels at 7.5 m to the track. Microphone #2, (a); Microphone #3, (b); Microphone #4, (c); Microphone #5, (d).

The measurements in a distance of 7.5 m to the track show (Figure 4.6):

- The highest extra noise is measured for the crossing nose at the track side in front of it (Microphone #3).
- For the crossing nose, the extra noise is clearly more important at the track side in front of it (Microphone #2 compared to Microphone #3). For the switch panel, the difference is not so important, and even slightly inverse: there is more extra noise at the track side opposite to the switch blade (Microphone #4 compared to Microphone #5).
- At the track side opposite to the turnout components, the extra noise levels are almost similar for the crossing nose and the switch panel (Microphone #2 compared to Microphone #4).

For L_{eq, T_p}^{Ref} between 90 dB and 95 dB, the extra noise levels for the crossing nose seem to follow a linear decrease with respect to L_{eq, T_p}^{Ref} (black arrows for Microphones #2 and #3). This can be interpreted as a source with a constant power being drawn in an increasing background noise. This tends to show that the noise at the crossing nose is more related to an impact noise due to the wheels passing over the gap. For the switch panel, in the same range for L_{eq, T_p}^{Ref} , the extra noise is more likely to be constant, or at least not following any clear linear decrease (black arrows for Microphones #4 and #5). This suggests that the extra noise is in this case more related to an increase of the rolling noise: same noise increase at the turnout for a train measured at 90 dB at the reference section than for another train measured at 95 dB.

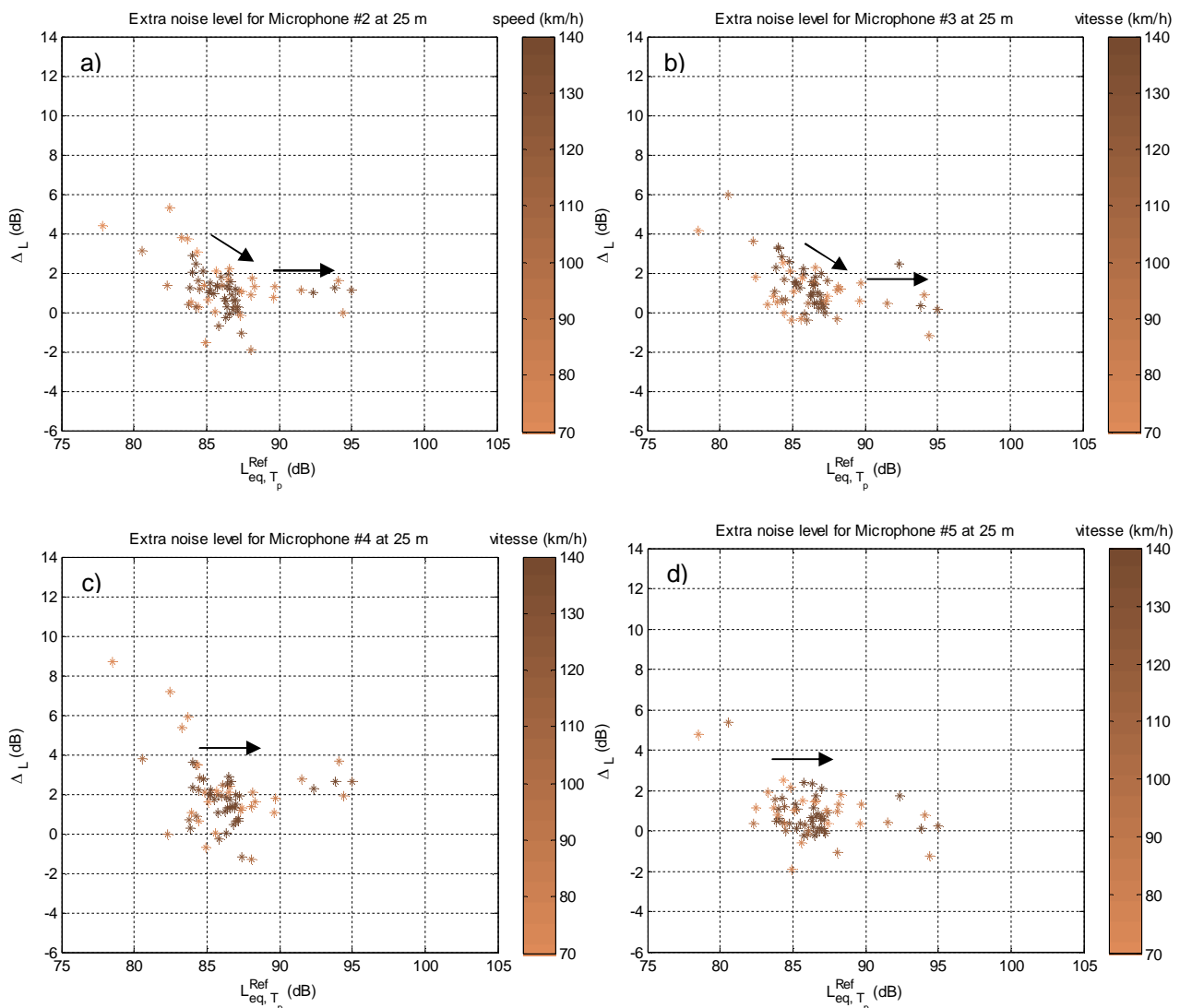


Figure 4.7: Extra noise levels at 25 m to the track. Microphone #2, (a); Microphone #3, (b); Microphone #4, (c); Microphone #5, (d).

At 25 m to the track (Figure 4.7), the influence of the impact noise source rapidly vanishes with L_{eq, T_p}^{Ref} and stays around a constant value which is the rolling noise increase (Microphones #2 and #3). For Microphones #4 and #5, only the rolling noise increase is measured.

ured. The impact noise source that is the crossing nose can be considered as a point source whose power is dissipated with the square of the distance to the source. As long as a train is noisy enough, the crossing nose contribution to the noise level at pass-by is almost none, especially far from the source. The rolling noise increase, which is more related to an extended source, is still present at 25 m to the track.

In order to support these hypothesis (crossing nose = impact and rest of the turnout = rolling noise increase), the averaged pass-by spectrum for a regional train is given in Figure 4.8 for Microphones #2 and #4. These results have been obtained by averaging the PSD computed for all regional trains with a speed around 140 km/h ($\pm 5\%$) and with the same number of axles.

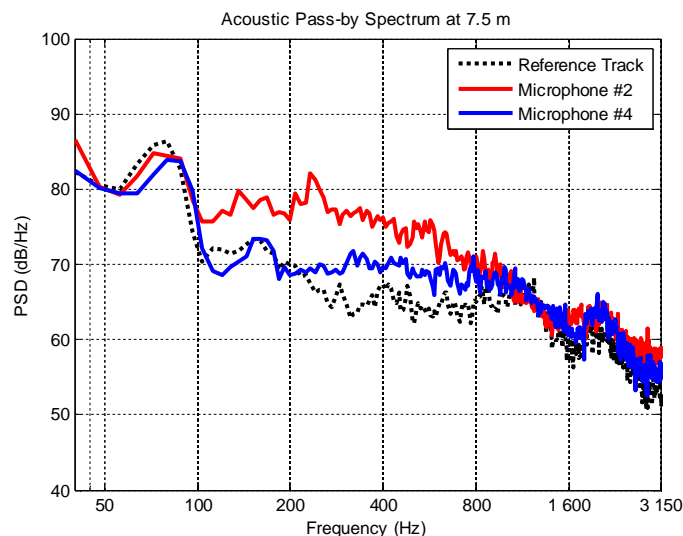


Figure 4.8: Averaged acoustic PSD at pass-by for regional trains.

It is clear that the noise increase in front of the crossing nose is broad band as the noise increase for the switch panel is more restricted to a “rolling noise” frequency band (200 Hz – 1000 Hz).

4.5 GROUND VIBRATION MEASUREMENTS

In this section the focus is on the Ground Vibration generation at 8 m and 32 m to the track. As for the noise in Section 4.4, in Figure 4.9 the extra ground vibration level Δ_L versus the reference level L_{eq, T_p}^{Ref} is plotted.

The only vibration increase is observed for the crossing nose at 8 m with an average around + 2dB. For the switch panel, and also far from the track for both sources, ground vibrations are strongly attenuated.

In Figure 4.10, the low frequency PSD of the rail acceleration at pass-by is plotted for two different types of train. In Figure 4.10 (left) the PSD of the rail acceleration is given for a freight train running at 70 km/h. In Figure 4.10 (right), the PSD of the rail acceleration is given for regional trains running at 140 km/h. From these spectra, it can be seen that the rail vibration above 50 Hz is more or less the same for the switch rail and the stock rail than for the reference section. Below this frequency, the rail vibration seems to be reduced for the switch rail and the stock rail compared to the reference section. This must be ana-

lysed with care as the accelerometers used are not really adapted for low frequencies. For the crossing nose acceleration, the same strong resonance as for the track receptance around 80 Hz (see Figure 4.4) can be found, and also a large increase of the levels above 25 Hz. This broad band increase results directly from the impact excitation at the crossing nose, responsible for higher rail excitations. For the other turnout components, the regular excitation mechanisms (unevenness and parametric excitation) are attenuated by the dynamic properties of the turnout.

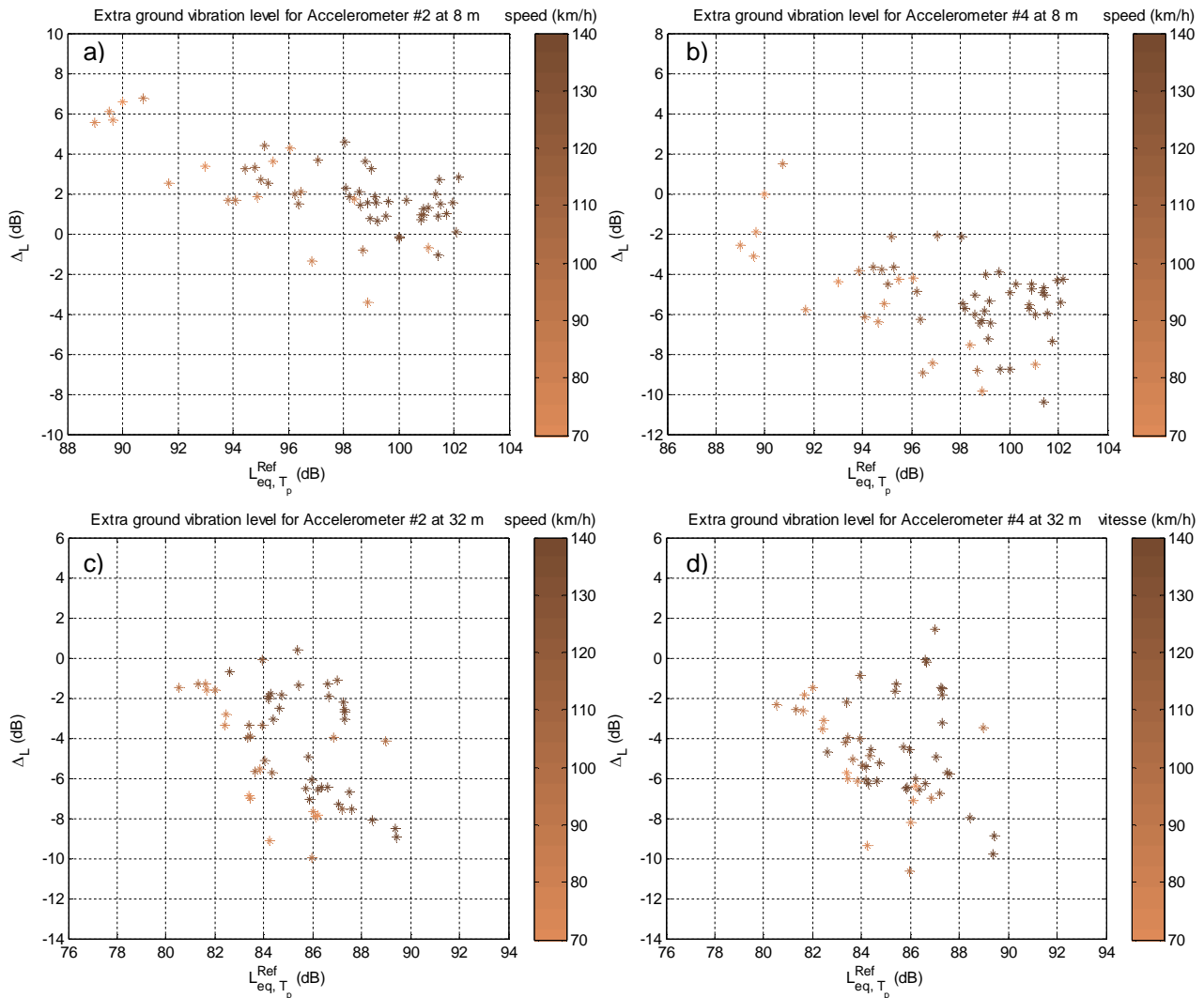


Figure 4.9: Extra ground vibration level. Crossing nose at 8 m (a); switch panel at 8 m (b); crossing nose at 32 m (c); switch panel at 32 m (d).

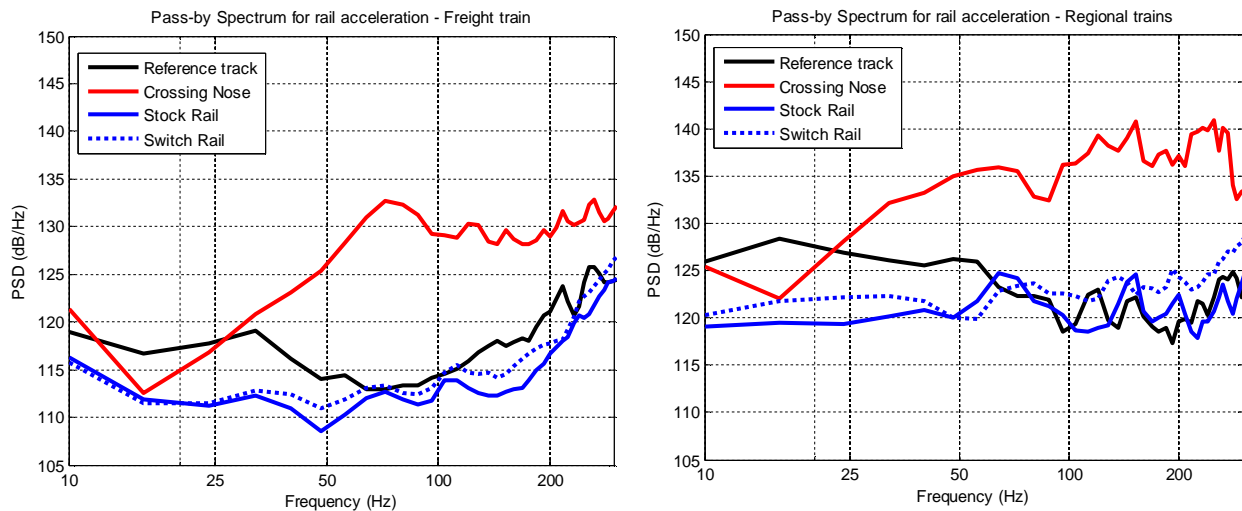


Figure 4.10: Low frequency pass-by spectrum for rail vertical acceleration. left: averaged over long freight train at $V=70$ km/h. right: averaged over all regional trains at $V=140$ km/h.

In order to complete and support this hypothesis, some further investigations might be needed:

- Analysis of the rail roughness along the turnout and the reference section, for long wavelengths in accordance to ground vibration. This will allow comparing the excitation due to unevenness on both sites.
- Using a low pass filter for the ground vibration signals before performing the extra level indicator. This will increase the signal to noise ratio for ground vibration and ensure that the indicator is not polluted by energy in higher frequency bands.
- Analysis of the soil characterization that was performed on both sites using multi-channel analysis of surface waves. This will give information on the soil capacity to transmit/attenuate ground vibration in some frequency bands.
- Analysis of the sleeper acceleration under the crossing nose for low frequencies (not available for the switch rail in our case).

4.6 CONCLUSIONS

The work presented in Chapter 4 is focused on a simple case within the complex issue that represent turnouts regarding noise and ground vibration. The problem is assessed for a turnout crossed by a mixed traffic, in the trailing move and for the direct route. By choosing these traffic conditions, the complex lateral excitations relative to the diverging route can be avoided. The two main sources studied here are the crossing nose and the location where the wheel/rail contacts jump from the switch rail to the stock rail. The crossing nose is obviously expected to act as an impulsive source due to the wheels passing over the frog. The jump from the switch rail to the stock rail may also be considered as an impulsive source, but not as strong as the source considered before.

This study first shows that many differences in the track design can be expected along the turnout compared to the surrounding regular track. On the test track within this investigation wooden sleepers are used versus concrete sleepers, different rail types are used (even along the turnout), and the fastening systems are different. This leads to different

dynamic behaviours of the track both for ground vibration related frequencies and for rolling noise related frequencies.

The low frequency track receptance under the crossing nose and under the switch jump was investigated for ground vibration. It showed a rather soft track under the switch jump and a strong resonance for the crossing nose at 80 Hz. The track stiffness was also found different for the switch rail and the stock rail, confirming that impact excitations may occur while wheels passing from one to the other. The high loads expected at the crossing nose were confirmed by the ground vibration levels measured at pass-by, higher than those at the reference section (at 8 m from the track). For train pass-bys with high vibration levels at the reference section, almost no increase is observed in front of the crossing nose. This supports the hypothesis of an impulsive source with a given power that can be drawn in the overall "vibration noise". However, the ground vibration levels measured at pass-by showed no increase at 8 m in front of the switch jump compared to the reference section. Attenuation was even found for all accelerometers at 32 m to the turnout (for the crossing nose, for the switch jump and also for an isolated joint which is present on the turnout but not discussed in this study). The soft design (possibly due to the wooden sleepers and to a higher ballast bed) of the turnout is responsible for this behaviour: it attenuates the vibrations which are due to regular excitation phenomena (quasi-static, parametric and unevenness excitation).

Increase of noise was measured for all microphones around the turnout. The crossing nose has been identified as a localized impact source with a given power, rather independent from the train reference noise. Its contribution to noise is especially important for silent trains and is higher at the side of the track where it is located (+1 dB at 7.5 m), see Figure 4.6. The influence of this source is very limited at 25 m to the track. In the 120-400 Hz frequency range, the track receptance shows higher mobility for the rail which contributes to rolling noise. This leads to an increase of the rolling noise along the turnout (around +2 dB at 7.5 m to the track and +1 dB at 25 m). This increase is also observed for noisy trains. In this frequency range, the main contribution to rolling noise comes from the track (and not the wheels), which is an extended source. Therefore this increase of rolling noise is also important at 25 m to the track.

These conclusions can be summarized with simple considerations:

- The crossing nose is a spatially isolated source of impacts, both for noise and ground vibration. Its contribution to annoyance along the track rapidly decreases with distance, and can be enhanced by track resonances.
- The track characteristics under this specific turnout are rather in favour of a reduction of ground vibration. The classical excitation mechanisms are mitigated, but it is not sufficient for the vibrations due to the impacts at the crossing nose. However, it has to be noticed that the variation of track global stiffness in turnout is generally pointed out as a cause of an increase of the wheel-rail interaction.
- The mechanical isolation tends to keep some energy in the rail which contributes to an increase of the rolling noise. The source is in this case extended, and its contribution to noise is still important at 25 m to the track.

The design of mitigation measures in a turnout could therefore consist in the following two objectives:

- the reduction of interaction force (train-track-interaction) along the turnout by smoothing the track global apparent stiffness along it (that was one of the idea of the USP in the Swiss project, see deliverable D3.6.)
- the reduction of impact load at the nose with for example a specific geometric design of the nose.

5. ASSESSMENT OF WHEEL-RAIL INTERACTION IN TURNOUTS BASED ON AXLEBOX MEASUREMENTS

The wheel-rail interaction along a turnout could be analysed with the measurement of axle box acceleration. This could give useful indications on the potential of wheel-rail interaction mitigation depending on the turnout designs.

SBB did a large and regular measurement campaign since 2007 (on 100% budget of SBB). The axle box acceleration measurements were analysed for train behaviour in curves and on straight line. Those collected measurement data contain also data³ from passages over several turnouts which are not relevant for the “regular usage”. It allows comparing the effect of different turnout designs on the interaction. It also allows checking the effect of USP installation in a turnout: can USP installed in a turnout smooth the global apparent stiffness along the track so that contact force is reduced?

5.1 AXLEBOX MEASUREMENTS

SBB has to measure tracks since May 2007 two times a year where train speed exceed 160 km/h. Therefore the track between Bern and Olten (NBS) and the tunnel of Lötschberg (LBT) are measured at maximum velocity with a test train. These regular tests consist also of lateral and vertical acceleration measurements at the axle boxes. These axle box measurements were also often performed between Bern-Thun since January 2009, in both directions, but as this is not a relevant track, no special velocities were ordered, and therefore the velocity profile is not identical.

The acceleration sensors az 11, az 12, az 41 and az 42 for the vertical accelerations at the axle boxes are shown in Figure 5.1, as an example of instrumentation together with other test measurements. At some of these test measurement campaigns wheels are equipped with strain gauges to measure dynamic wheel-rail contact forces.

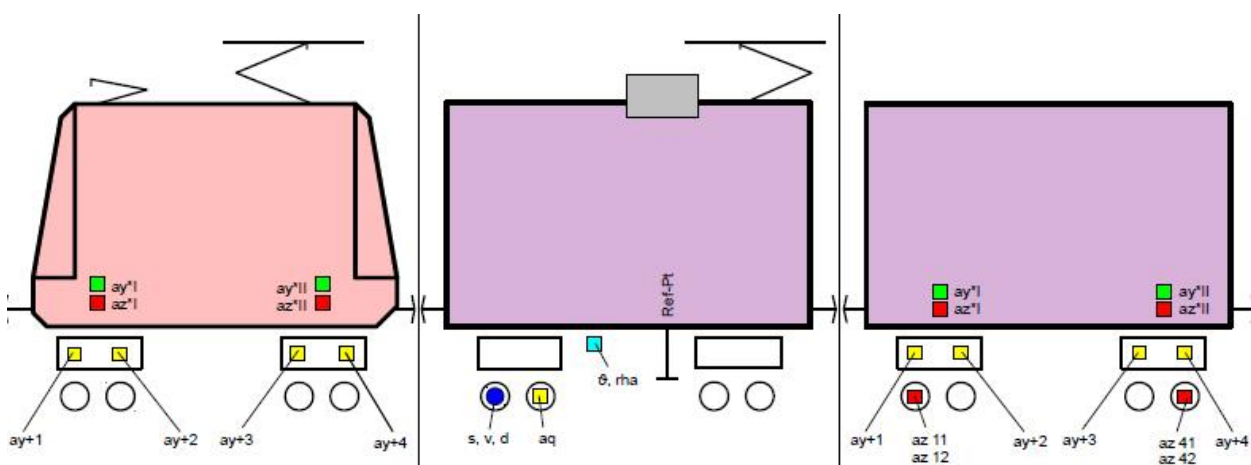


Figure 5.1: Example of instrumentation of measurement 4.7.2013.

³ Those data was evaluated and analysed within RIVAS. So it was possible to use existing data over 5 years for further investigations in RIVAS without needing budget for such measurements providing that data.

The measurement wagon EW IV (last wagon in Figure 5.1) was always the same since 2007-January 2013, only used for these measurements. But since summer 2013, the last measurement campaign, the wagon has to be hired and is in use (changes in OOR conditions). In Figure 5.2 the sensor to measure vertical accelerations of the axle box (as well as lateral accelerations) is visible. Setra 131A sensors with a range of 30g were used to measure the vertical acceleration levels.

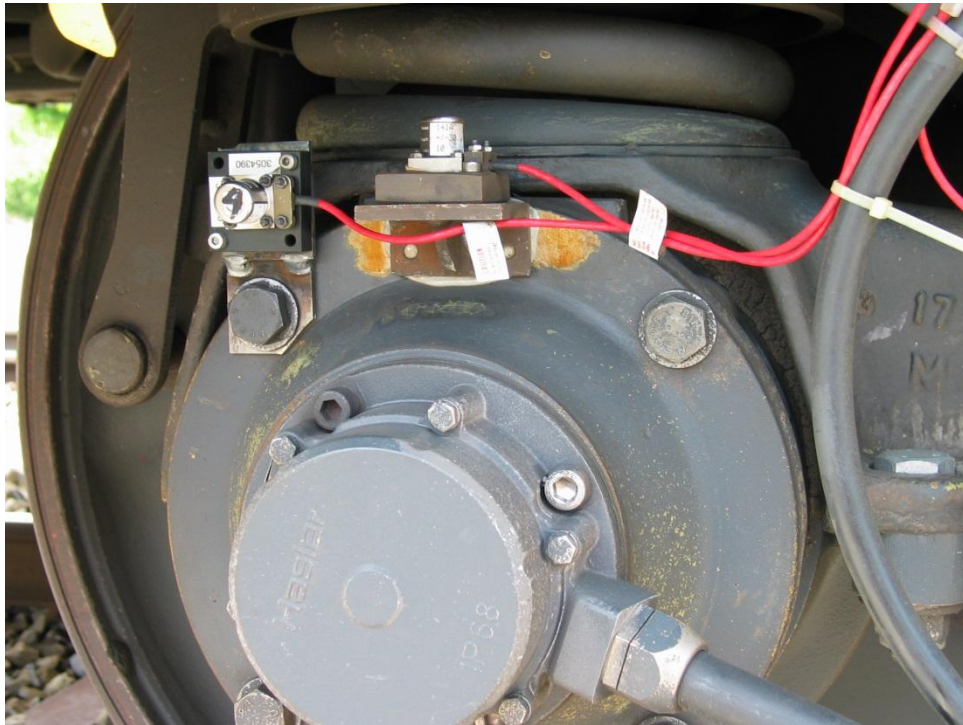


Figure 5.2: Vertical acceleration sensor (as well as lateral acceleration sensor) on axle box

Signal processing:

The signal processing was performed with a developed software (“SM2S”) for technical train test runs. All input signals are filtered with an antialiasing filter, Butterworth low pass of 200 Hz, at a sampling frequency of 1000 Hz (saving measurement data every 0.001 s).

5.2 ANALYSIS OF MEASUREMENTS

Axle box acceleration measurement data, acquired with the set-up described in Section 5.1, were post-processed to investigate the acceleration levels for different turnout locations, turnout types (i.e. radius, with/without USP) and the influence of maintenance work and wear on the resulting axle box acceleration levels during a turnout crossing.

The turnout crossing speed was not the same for the different data sets and therefore the measured peak acceleration levels, a_{peak} , are in some diagrams linearly scaled⁴ with the

⁴ Maximum acceleration levels based on an impulse excitation are assumed to correspond to a $\Delta z/\Delta t$. Δz as the geometrical irregularity in vertical direction is assumed to be constant. $1/\Delta t$ is proportional to the actual train crossing speed. Therefore, maximum acceleration levels are linearly scaled with velocity (relative to nominal speed to preserve units of acceleration). In Figure 5.11 for Nov. 2011 and Rubigen Turnout 1, the very low train velocity seems perfectly corrected by the linear scaling.

actual train speed during turnout overrun, v , relative to the nominal crossing speed $v_0=160$ km/h:

$$a_{\max, \text{corr}} = a_{\text{peak}} \cdot (v_0/v)$$

Equation 1: Crossing speed correction for peak acceleration levels

Table 5.1: Turnout crossing speeds during axle box acceleration measurements

Turnout No	Rubigen 1	Rubigen 2	Rubigen 11	Rubigen 12	Wichtrach 1	Wichtrach 9	Wichtrach 20
Jan 2009	150 km/h	160 km/h	160 km/h	160 km/h	145 km/h	145 km/h	155 km/h
May 2009	160 km/h	160 km/h	160 km/h	160 km/h	160 km/h	160 km/h	160 km/h
Nov 2009	150 km/h	150 km/h	150 km/h	150 km/h	160 km/h	160 km/h	160 km/h
Jun 2010	155 km/h	155 km/h	150 km/h	155 km/h	155 km/h	155 km/h	160 km/h
Apr 2011	135 km/h	150 km/h	155 km/h	160 km/h	160 km/h	160 km/h	160 km/h
Nov 2011	40 km/h	40 km/h	40 km/h	40 km/h	50 km/h	35 km/h	55 km/h
Apr 2012	155 km/h	160 km/h	155 km/h	160 km/h	160 km/h	160 km/h	160 km/h
Jul 2012	155 km/h	160 km/h	160 km/h	160 km/h	160 km/h	160 km/h	160 km/h
Jan 2013	155 km/h	160 km/h	160 km/h	160 km/h	160 km/h	160 km/h	160 km/h
Jul 2013	85 km/h	160 km/h	125 km/h	125 km/h	160 km/h	160 km/h	160 km/h

The localization of the main impulse and especially the temporal variation due to turnout wear or maintenance work from the turnout on the vehicle could not be defined accurate enough with a typical crossing speed of approx. 160 km/h and a sampling rate of 1 kHz due to the resulting spatial resolution of about 0.044 m.

5.2.1 Investigated test sites

For the present report, acquired acceleration data for turnouts in Rubigen and Wichtrach on the line between Bern and Thun were analysed (see Figure 5.3). In Rubigen there are two turnouts with under sleeper pads ($c_{\text{stat}} = 0.22$ N/mm³) and two turnouts without under sleeper pads. The four turnouts in Rubigen are all of the EW VI-900-G/B-1:19-F/Be,R(T) type.

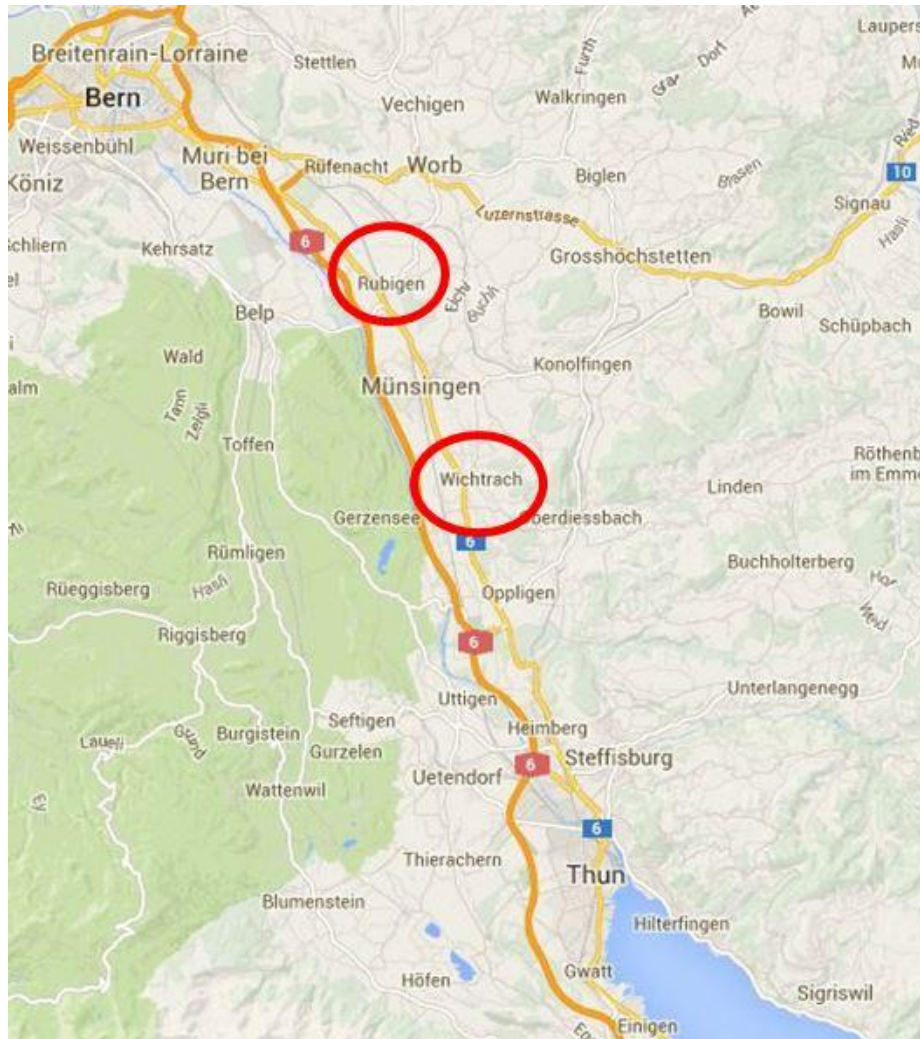


Figure 5.3: Test sites in Rubigen and Wichtrach between Bern and Thun (Digital Map Data ©2014 GeoBasis-DE/BKG (©2009), Google)

In Section 5.2.2 acceleration sensor raw data will be presented for consecutive turnout crossings from January 2009 until July 2013. Resulting acceleration levels on the axle box will be discussed and comparison between right and left side of the axle for the lateral as well as for the vertical directions will be done.

Acceleration sensor signals are illustrated relative to the absolute track location. However, as the track location is recorded relative to its initialization point at the beginning of the measurement run, absolute numbers have therefore to be handled with care. For the present investigation the exact localization of the main impulse from the track system on the vehicle and the temporal change of the location of maximum interaction are not of major interest due to the spatial resolution of about 0.044 m at a sampling rate of 1 kHz. The absolute track location therefore was not re-calibrated using characteristic and well defined track irregularities in the close vicinity of the investigated turnouts.

The time series from years 2009 to 2013 is sometimes incomplete due to a malfunction of the corresponding sensor sets.

5.2.2 Spatial resolution

The effect of the sampling rate of 1 kHz and an anti-aliasing filter at 200 Hz on the measured acceleration levels is visible in Figure 5.4. The illustration shows the raw signal of the vertical acceleration levels for two crossings over the same turnout. With a crossing speed of 40 km/h the higher spatial resolution of about 1 cm results in a more detailed temporal representation of the dynamic interaction. Therefore the rms-values before and after the turnout impulse show different levels. The lower spatial resolution for a crossing speed of 150 km/h results in a low-pass filtering effect.

Figure 5.5 shows the corresponding frequency content in the two raw signals illustrated in Figure 5.4. The spatial and frequency resolution at nominal crossing speed points out the need for axle box acceleration measurements performed with higher sampling rates to investigate the dynamic interaction of the vehicle with different turnout configurations and its temporal evolution in more detail.

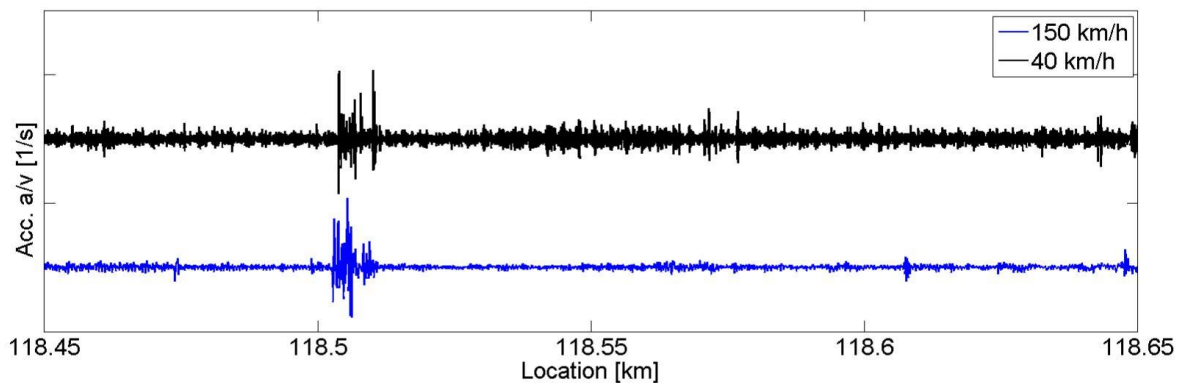


Figure 5.4: Speed dependent spatial resolution at 1 kHz sampling rate, vertical acceleration (scaled with train velocity according to Eq. 1), Turnout 1, Rubigen

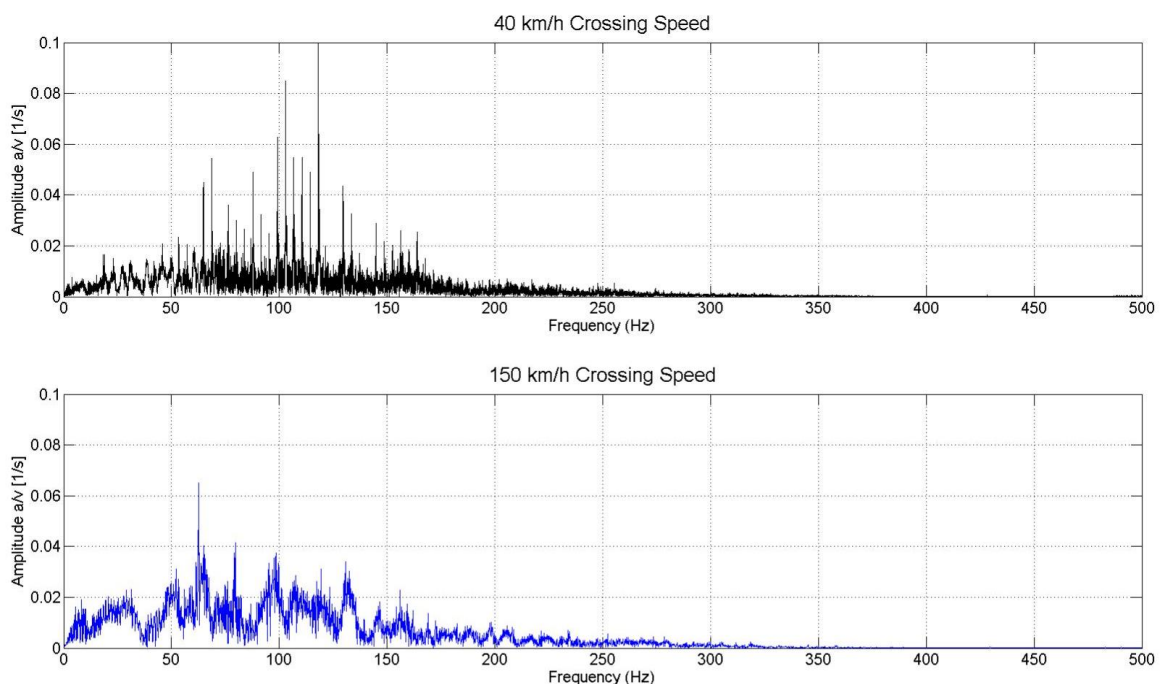


Figure 5.5: Speed dependent frequency content at 1 kHz sampling rate, vertical acceleration (scaled with train velocity according to Eq. 1), Turnout 1, Rubigen

5.2.3 Measurement data for Rubigen test site

In Figure 5.6 and Figure 5.7 lateral acceleration levels of axle boxes for the first wheel set are illustrated. In Figure 5.6 resulting acceleration levels are presented for the right side of the axle whereas in Figure 5.7, presented acceleration levels correspond to the left side of the axle. In general, the maximum acceleration levels are larger on the right axle by a factor of about 1.2 – 1.5. However, as the sensors are located on the same axle, lateral acceleration levels are expected to show a smaller deviation than the factor of 1.2 – 1.5. The difference might be interpreted as measurement uncertainty caused by the set-up/sampling rate. Acceleration levels before and after the turnout tend to decrease over the years by a factor of about 2, the reason is not yet identified.

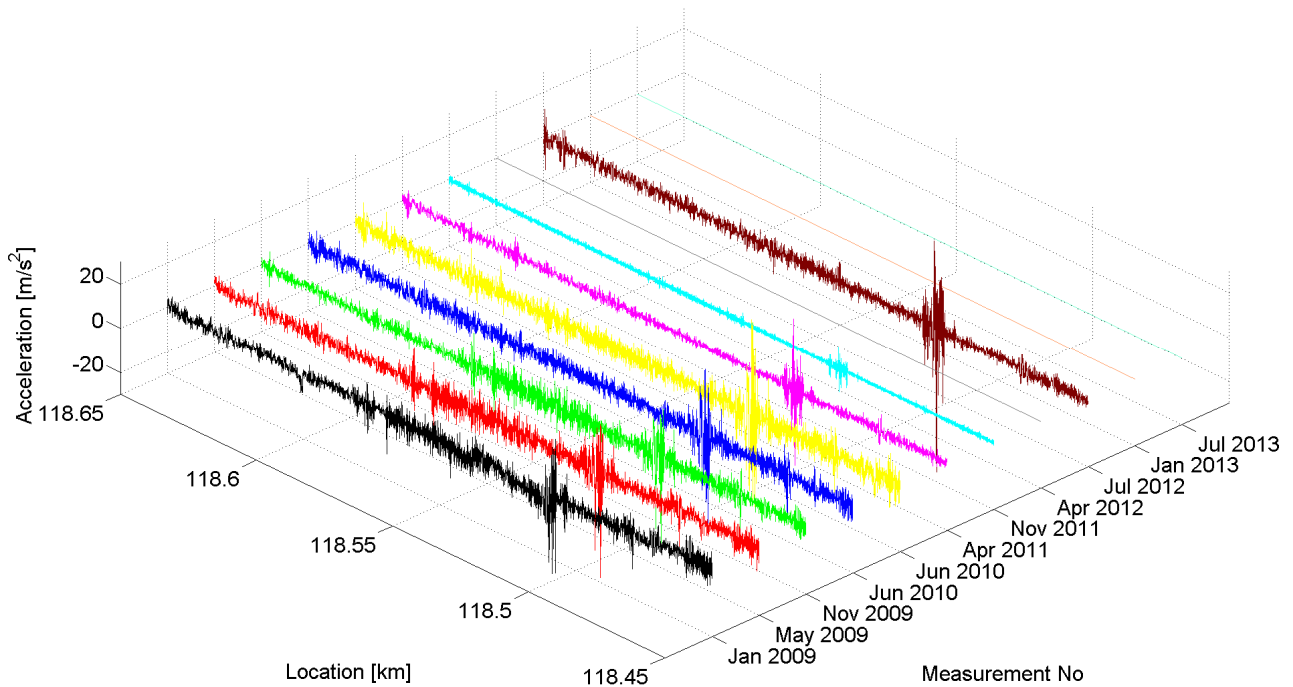


Figure 5.6: Rubigen Turnout 1, lateral acceleration, axle box 1, right side

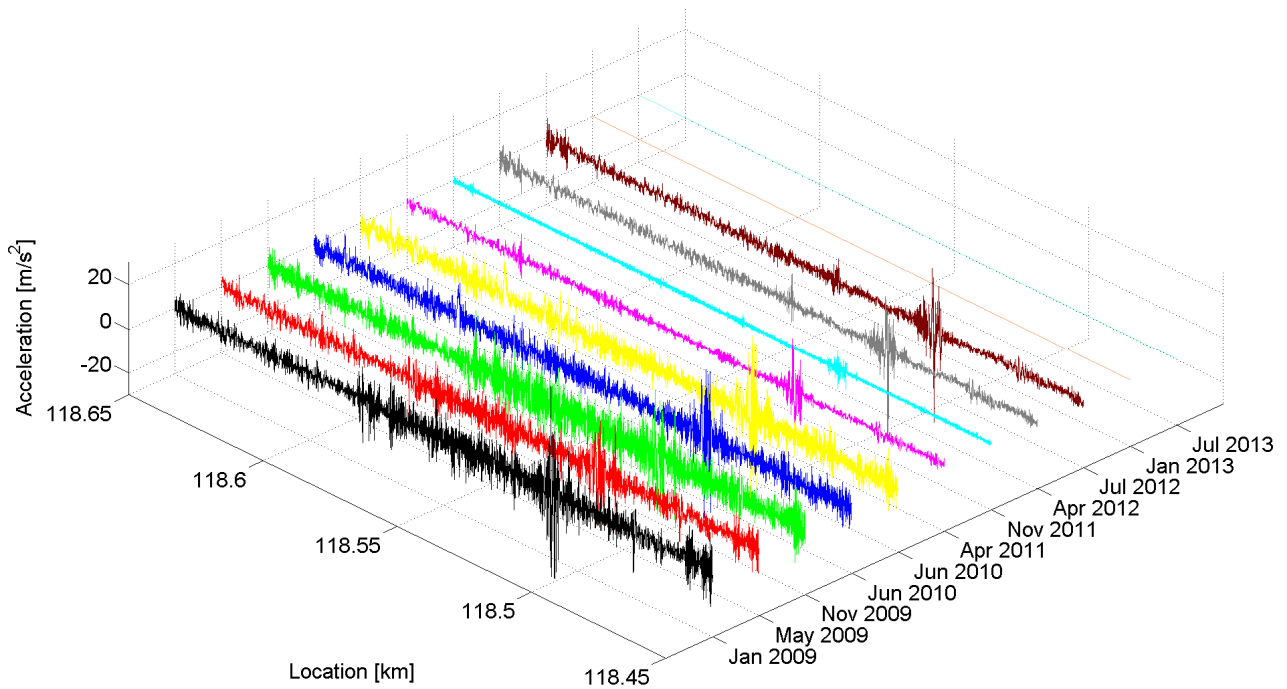


Figure 5.7: Rubigen Turnout 1, lateral acceleration, axle box 1, left side

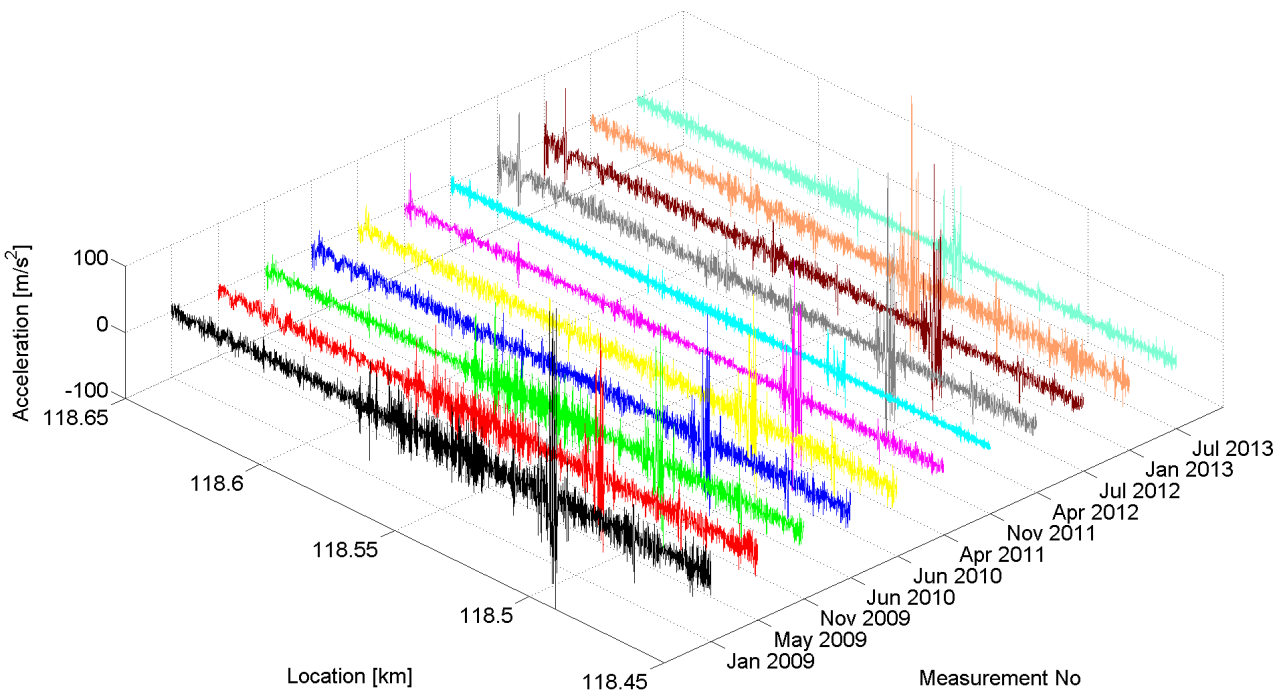


Figure 5.8: Rubigen Turnout 1, vertical acceleration, axle box 1, right side

In Figure 5.8 and Figure 5.9 vertical acceleration levels of axle boxes of the same wheel set are illustrated for the first axle, for the left as well as for the right axle box. In Figure 5.8 resulting acceleration levels are presented for the right side of the axle. Figure 5.9 shows the acceleration levels for the left side on the same axle. Vertical acceleration levels in general are larger by about 30% - 50% on the right side of the axle before and after the

turnout. This systematic difference indicates that the wheel tread surfaces probably are not in the same condition, but no wheel OOR measurements are available. Focussing on the interaction between turnout and vehicle in vertical direction, acceleration levels are larger by a factor of about 2.2 on the right side of the axle.

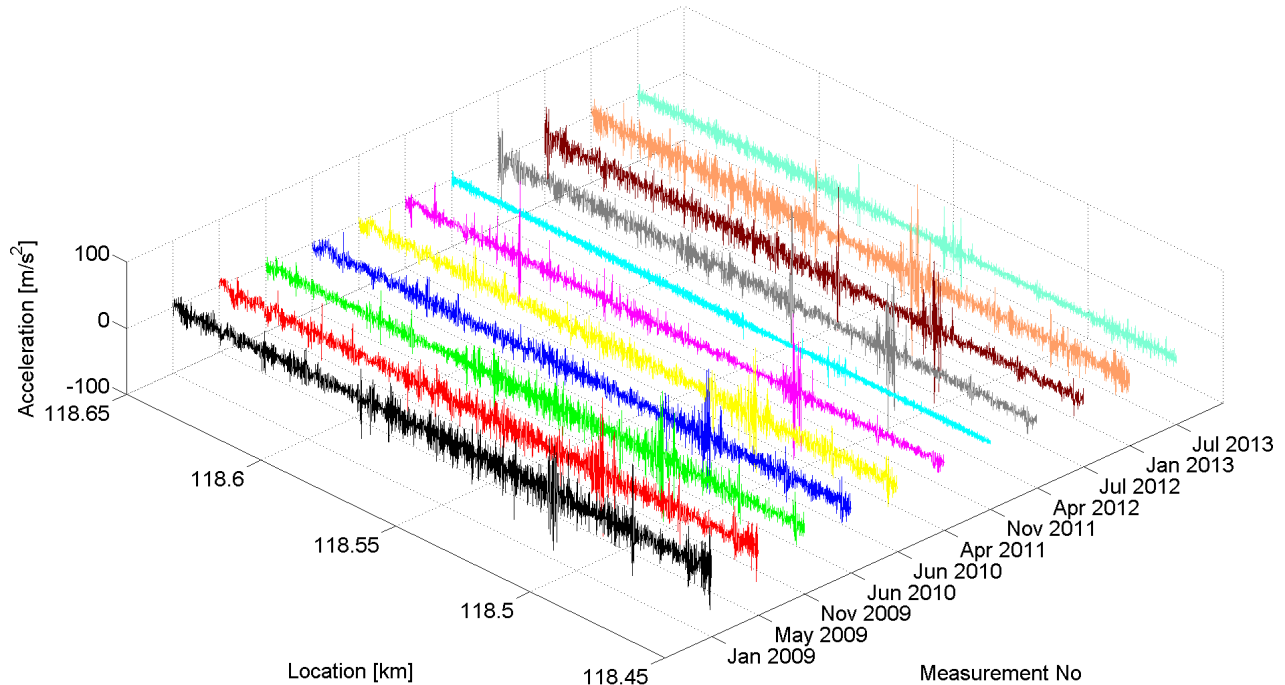


Figure 5.9: Rubigen Turnout 1, vertical acceleration, axle box 1, left side

It can clearly be seen that for the measurements performed in January and July 2013 the track location measurement system shows an offset of about 25 m when compared to the measurements performed from 2009 to 2012.

As a last raw data set, the measured acceleration levels for the bogie in lateral direction are shown in Figure 5.10. The peak acceleration levels show a linear increase over the years. The effect of the sampling rate on the measured maximum acceleration level is visible in the measurement performed in November 2011 with a reduced turnout crossing speed (40 km/h instead of 150 – 160 km/h).

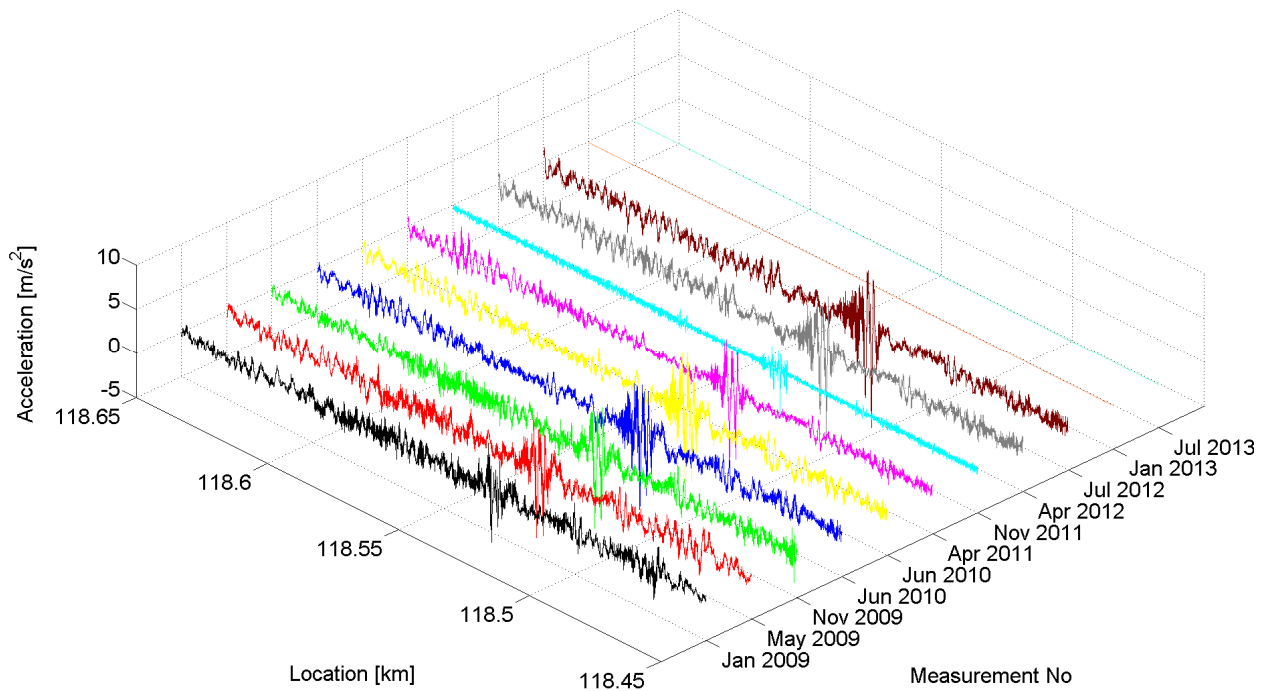


Figure 5.10: Rubigen Turnout 1, lateral acceleration bogie

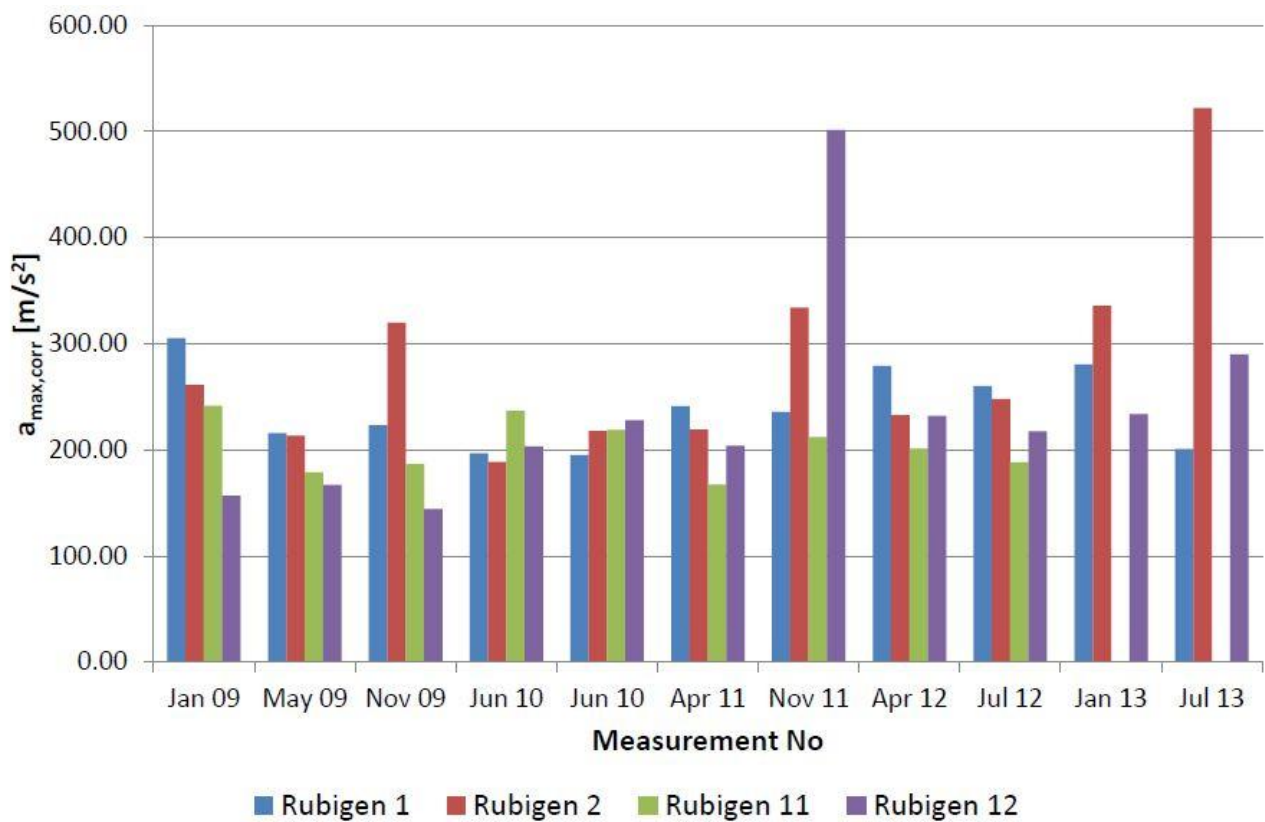


Figure 5.11.a: Rubigen, crossing-speed corrected max acceleration levels, vertical direction, right side

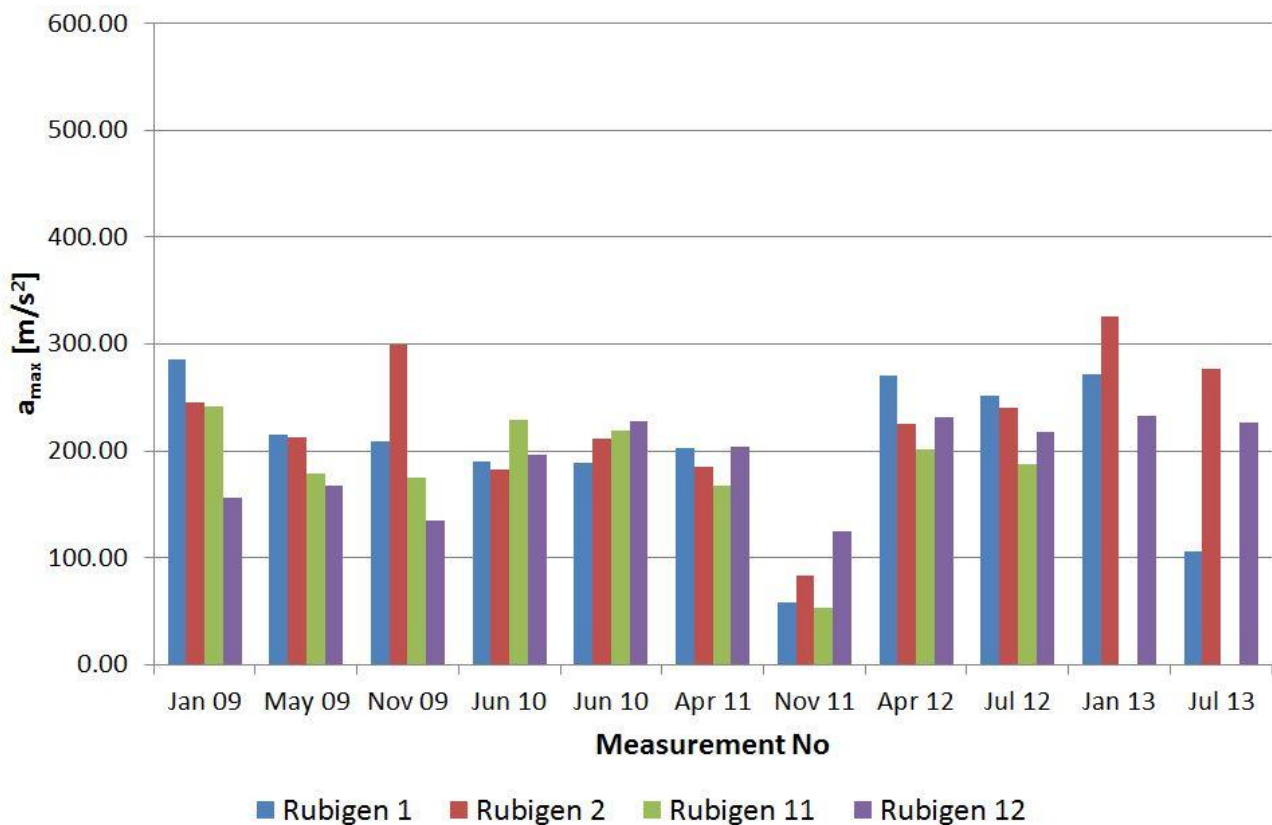


Figure 5.11.b: Rubigen, max acceleration levels, vertical direction, right side

In Figure 5.11.a the crossing-speed corrected maximum acceleration levels, according to Equation 1, in vertical direction for the four turnouts in Rubigen are illustrated. Figure 5.11.b shows the uncorrected maximum acceleration levels. It is obvious that lower turnout crossing speeds result in lower maximum acceleration levels. The scaling of the measured maximum acceleration level with the turnout crossing speed does not result in a more systematic distribution of the peak acceleration levels for the different turnouts under investigation. The data set does not allow drawing conclusions about the influence of under sleeper pad on the resulting maximum acceleration levels in vertical direction (see for USP also Chapter 5.2.6). Furthermore, no temporal evolution of the turnout-vehicle interaction can be seen over the measurement period from January 2009 to July 2013, possibly because of the low spatial resolution due to the relatively low sampling frequency.

5.2.4 Measurement data for Wichtrach test site

In Wichtrach (see Figure 5.3) five turnouts, two with under sleeper pads, two without under sleeper pads and one turnout with a radius of 300 m, are installed. Turnout 1 in Wichtrach is an EW VI-900-G-1:19-F/Be,R type with under sleeper pads, Turnout 20 is an EW VI-900-G-1:19-F/H,L(T) type without USP and Turnout 9 is an EW VI-300-G-1:19-F/Be,R(T) type. In November 2012 Turnout 1 in Wichtrach was replaced by the newly developed “Weiche 2015” which should be the standard turnout in the future and was developed to improve maintenance and a longer lifetime.

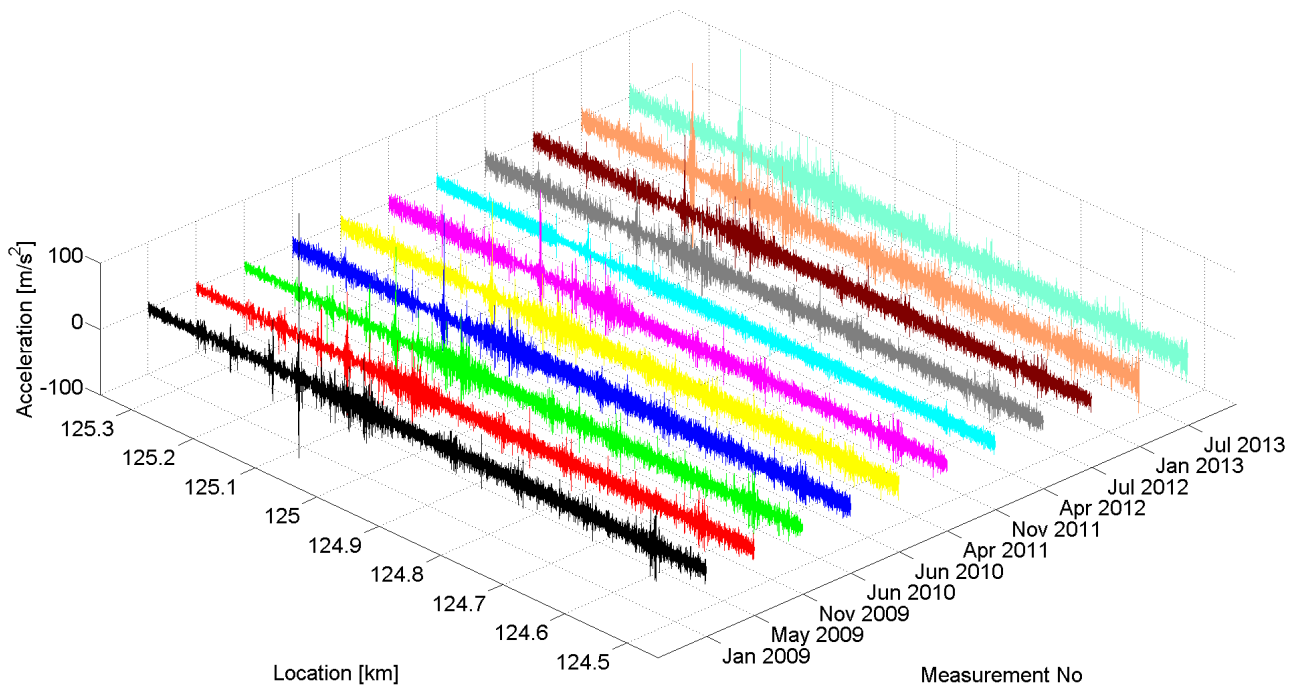


Figure 5.12: Wichtrach Turnout 1, vertical acceleration, axle box 1, right side (from January 2013 data is shown for “Weiche 2015”).

The acceleration values before and after Turnout 1 with under sleeper pads are larger when compared to Turnout 20 without under sleeper pads as illustrated in Figure 5.12 and Figure 5.13. The reason for this difference in track behaviour is not found yet.

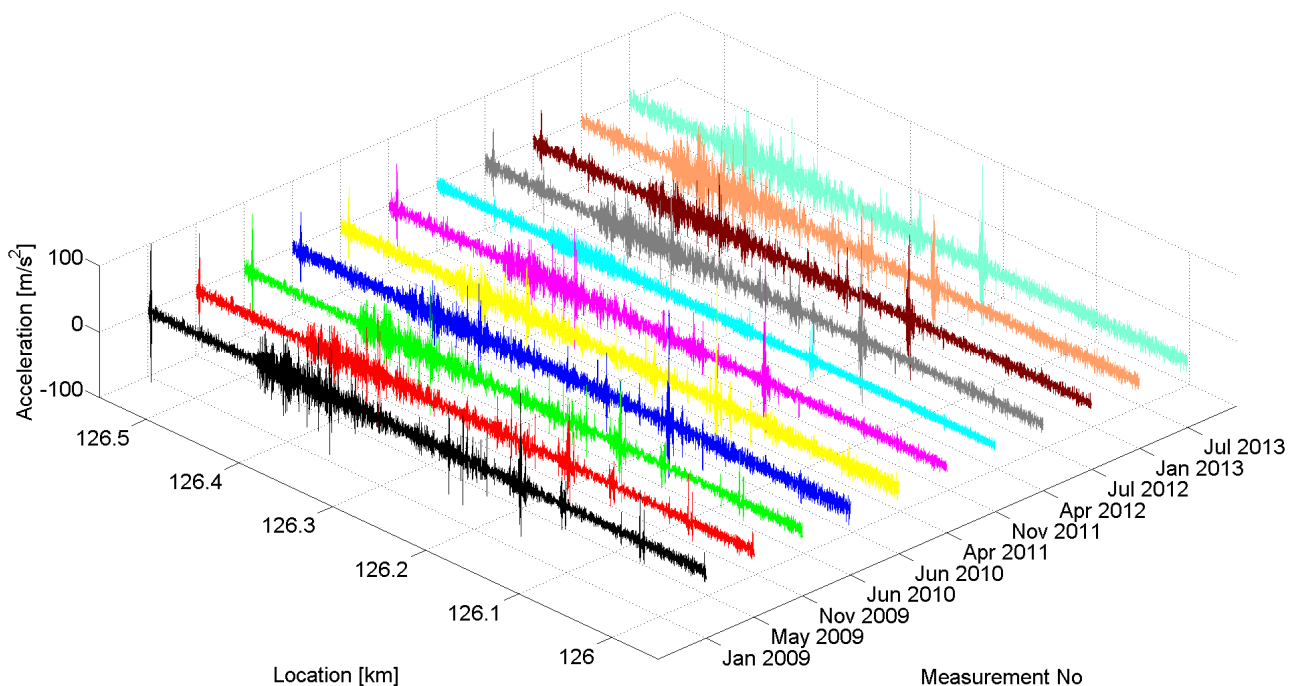


Figure 5.13: Wichtrach Turnout 20, vertical acceleration, axle box 1, right side

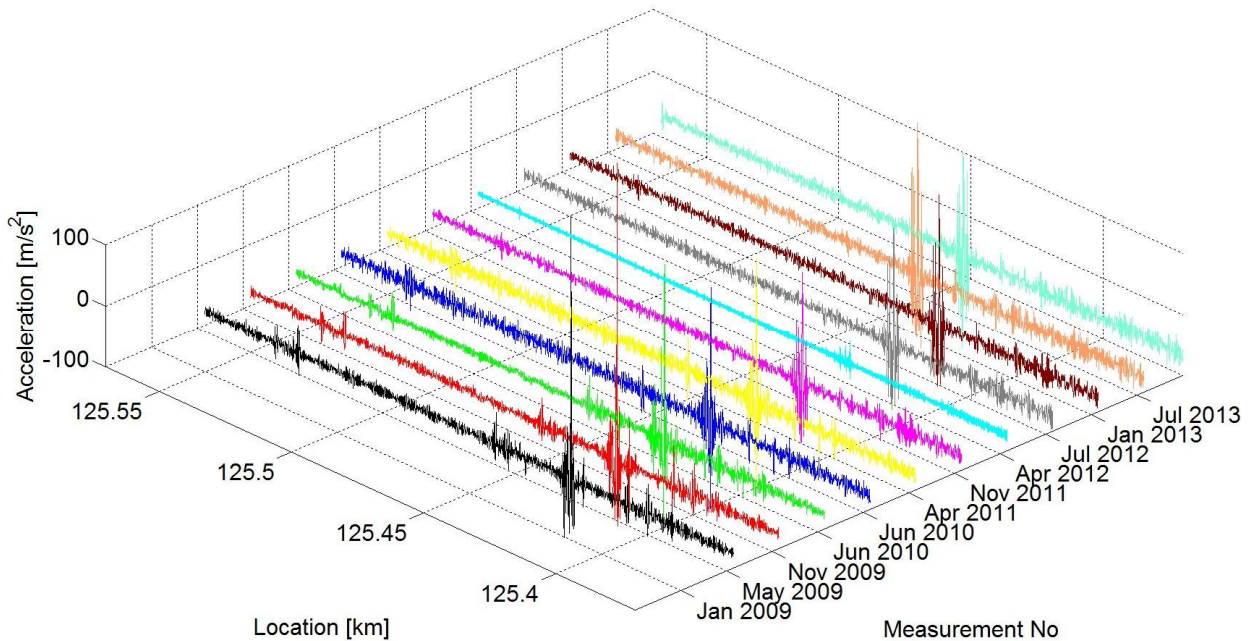


Figure 5.14: Wichtrach Turnout 9, vertical acceleration, axle box 1, left side

For Turnout 9 in Wichtrach with a 300 m radius the calculated crossing-speed corrected maximum acceleration levels during turnout crossing are generally larger as shown in Figure 5.15.a as well as in Figure 5.15.b. This is in accordance with the conclusion of deliverable D3.6 that a smaller radius turnout generates more vibration. Maximum acceleration levels for Turnout 1 and Turnout 20 in Wichtrach show no systematic trends to be put in correlation with maintenance.

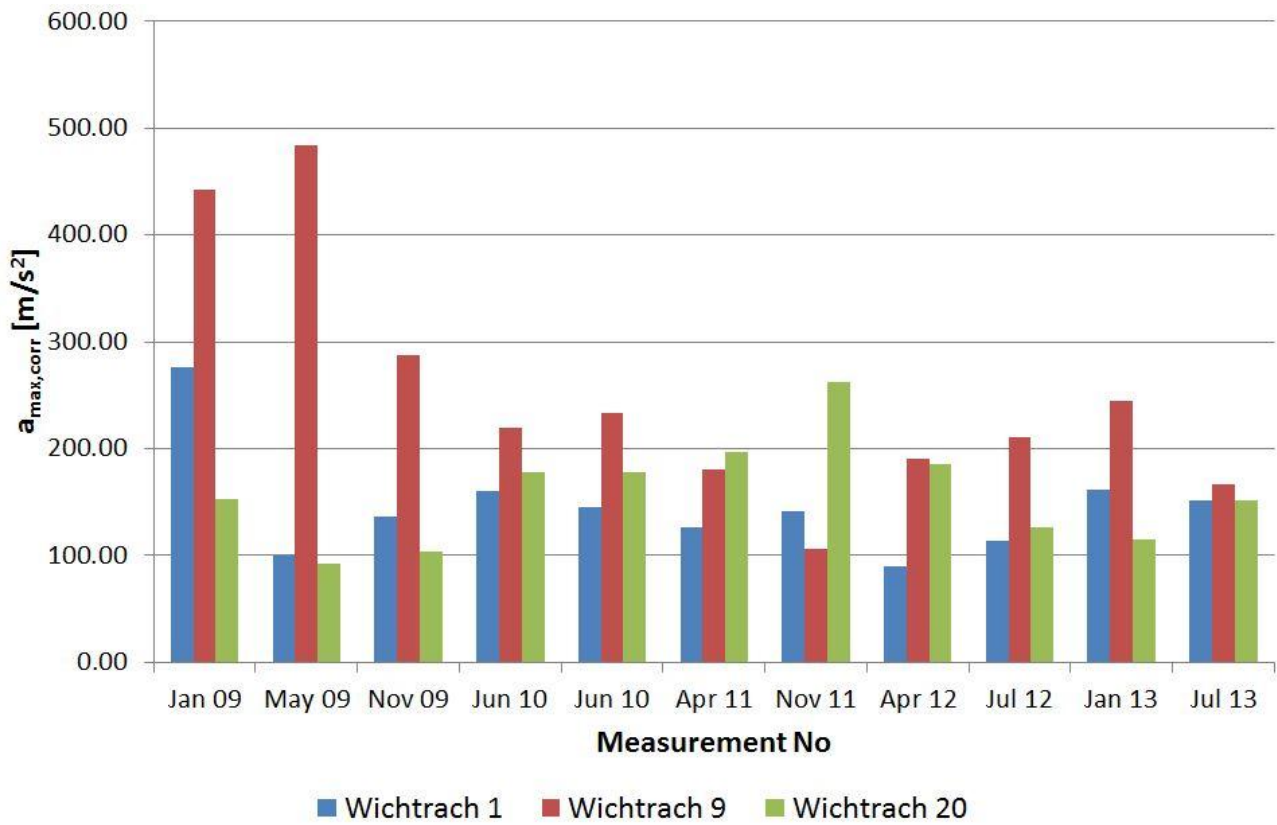


Figure 5.15.a: Wichtrach, crossing-speed corrected max acceleration level, vertical direction, right side

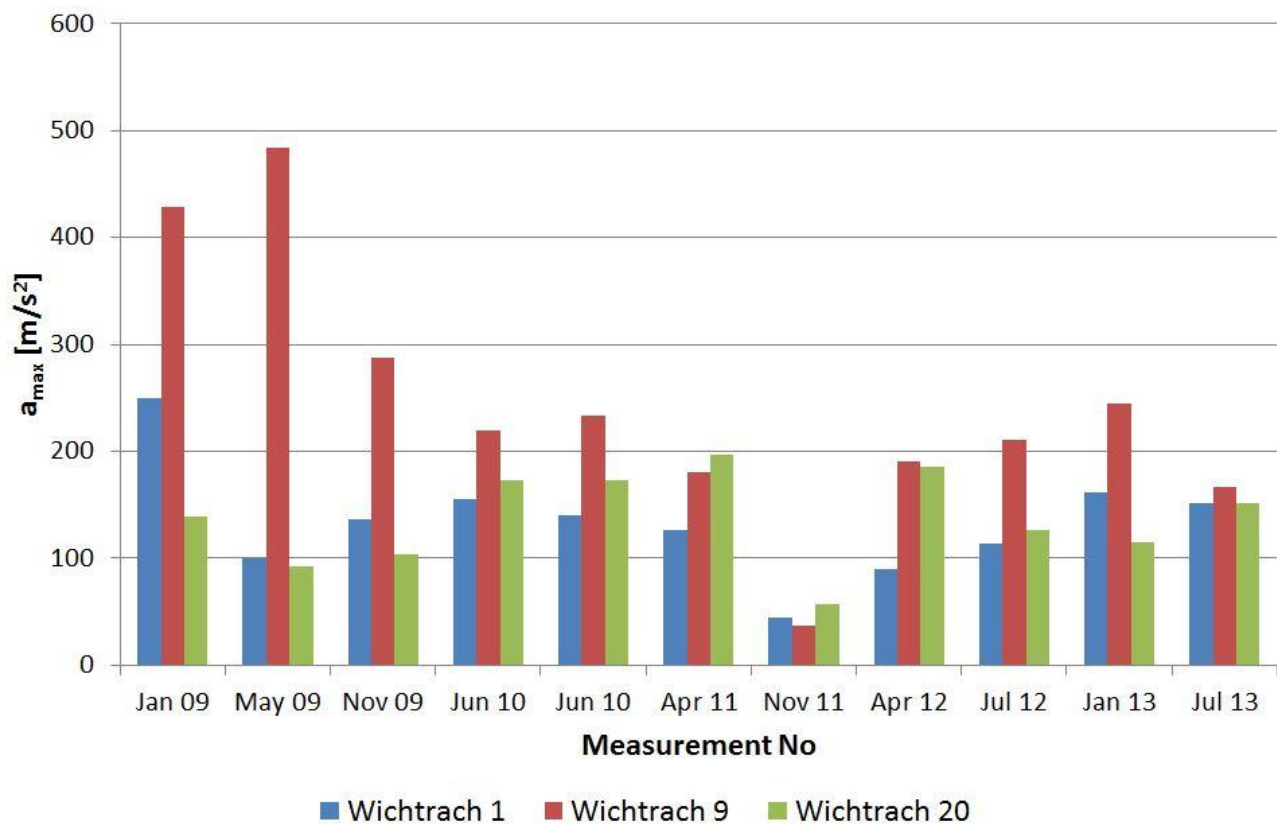


Figure 5.15.b: Wichtrach, maximum acceleration level, vertical direction, right side

5.2.5 Integral quantities for the comparison of different turnout designs

In this section, the comparison for different turnout locations, turnout types and track characteristics is done based on integral quantities (no application of pass-by-speed correction applied). Before as well as after the turnout a root-mean-square value, rms, is used to quantify the track quality in the close vicinity of the turnout and to define the zone of interaction as shown in Figure 5.16. Within the zone of interaction, the normalized impulse energy is calculated. Normalization was done based on the maximum impulse energy calculated for Turnout 2 in Rubigen (measurement performed in January 2013, see Figure 5.17).

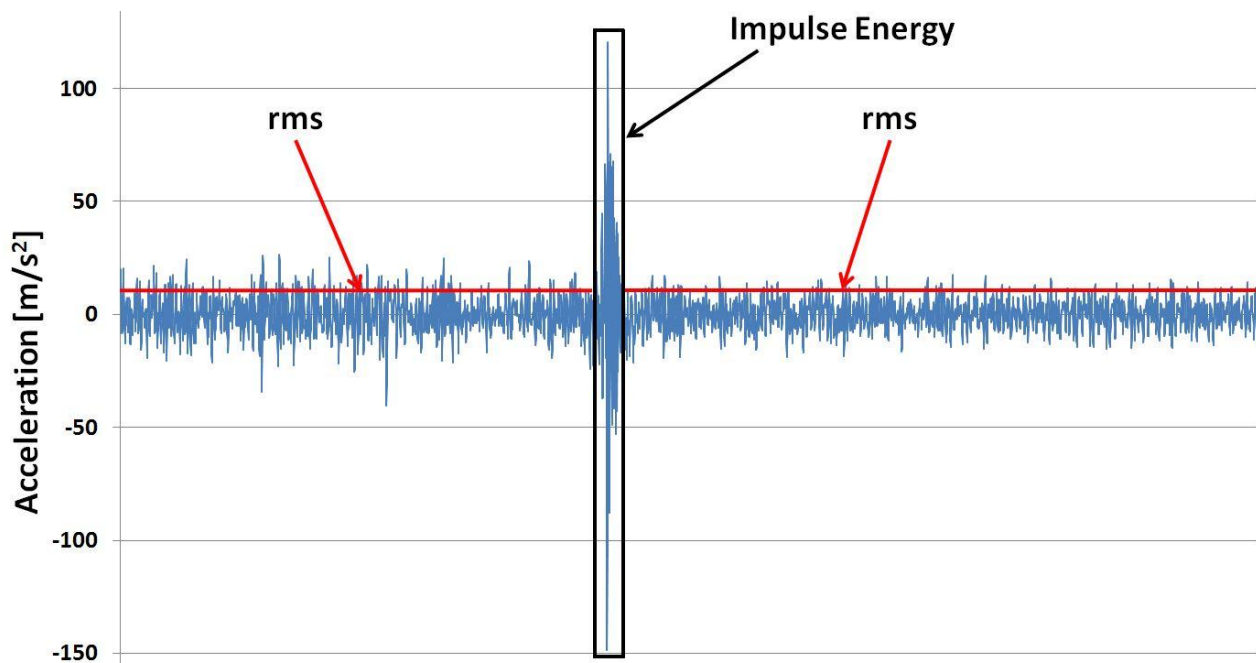


Figure 5.16: Integration of turnout-vehicle interaction

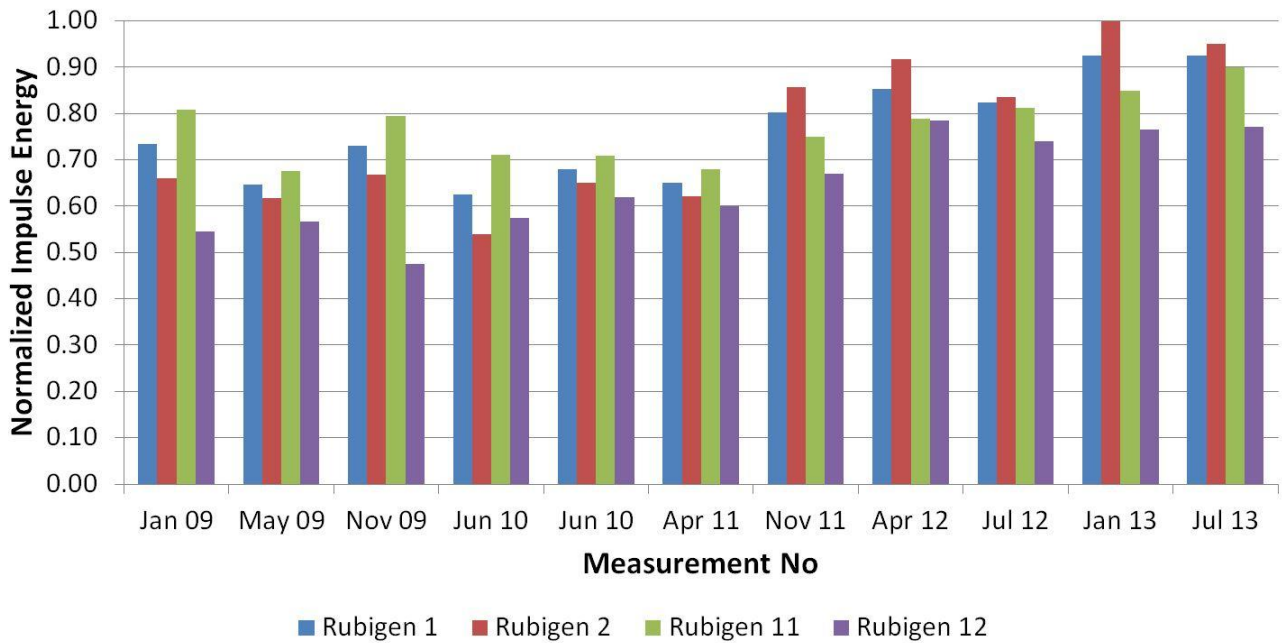


Figure 5.17: Rubigen, normalized impulse energy in vertical direction, right side

Figure 5.17 shows the normalized impulse energy for the four turnouts in Rubigen (Rubigen 1 and 2 with USP, Rubigen 11 and 12 without USP). It can be seen that Turnout 12 caused lowest interaction levels. This is in well agreement with findings reported in [1] where lower frog acceleration levels were measured for Turnout 12 when compared to Turnouts 1, 2 and 11. The measured frog acceleration levels are shown in Figure 5.18.

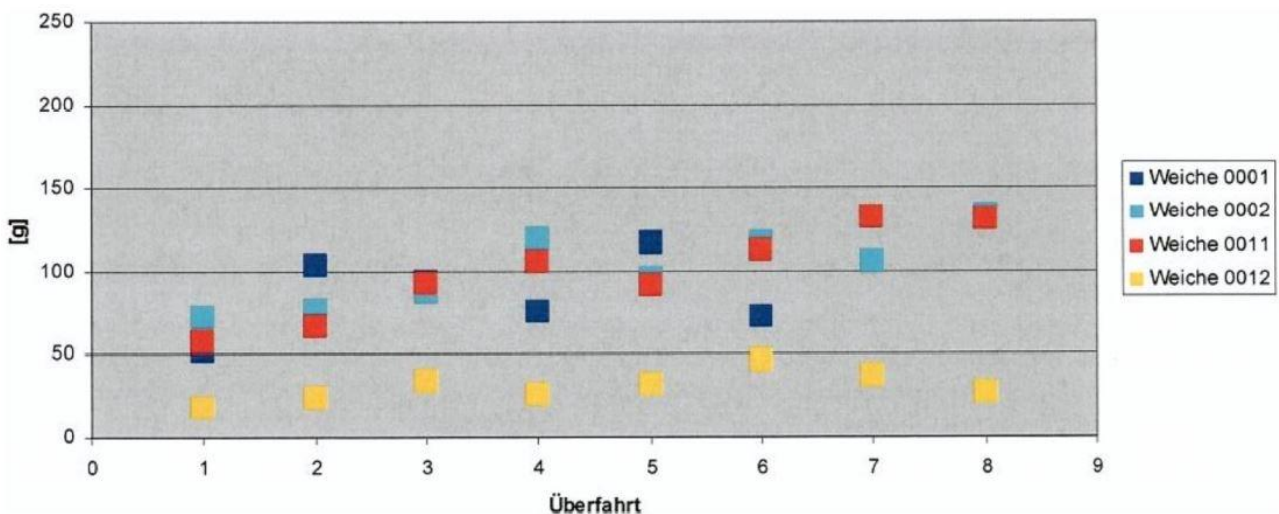


Figure 5.18: Rubigen, frog acceleration levels from [1]

Figure 5.19 shows the normalized impulse energy for the three turnouts in Wichtrach. Turnout 9 with a radius of 300 m resulted in highest interaction levels when compared to Turnout 1 and Turnout 20 with a radius of 900 m.

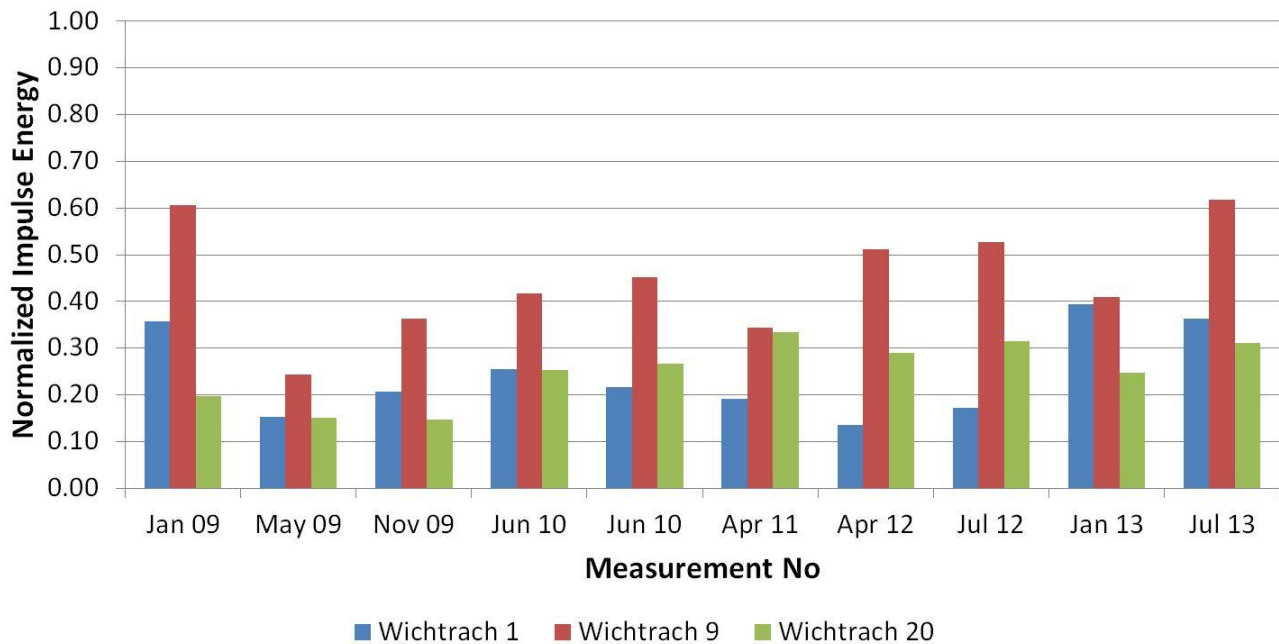


Figure 5.19: Wichtrach, normalized impulse energy in vertical direction

Normalized impulse energy levels are lower for the turnouts in Wichtrach when compared to the Rubigen test site, illustrated in Figure 5.17.

5.2.6 Effect of under sleeper pad on acceleration levels

Turnout 1 and 2 in Rubigen as well as Turnout 1 in Wichtrach are equipped with under sleeper pads ($c_{\text{stat}} = 0.22 \text{ N/mm}^3$). The comparison of the maximum as well as of the impulse energy levels does not indicate any influence of the under sleeper pads on the dynamic turnout-vehicle interaction. An explanation might be the frequency dependent dynamic stiffness of the under sleeper pads. However, turnouts with under sleeper pads tend to show higher rms-levels before and after the turnout.

5.2.7 Effect of turnout radius on lateral acceleration levels

Besides the vertical acceleration levels, for a turnout with a small radius the lateral acceleration amplitudes might be of special interest when compared to a turnout with a radius of 900 m.

In Figure 5.20 the measured lateral acceleration levels are shown for Turnout 9 in Wichtrach with a radius of 300 m. In Figure 5.21 the same data is shown for Turnout 20 with a radius of 900 m.

The lateral axle box acceleration levels are larger by a factor of about 2 for the turnout with the small radius of 300 m when compared to the turnout with a radius of 900 m. Values

tend to decrease over the years for Turnout 9 whereas for Turnout 20 the maximum acceleration amplitudes in lateral direction are stable from 2009 to 2013. For Turnout 20 in Wichtrach, no significant difference in terms of axle box acceleration levels were found so far.

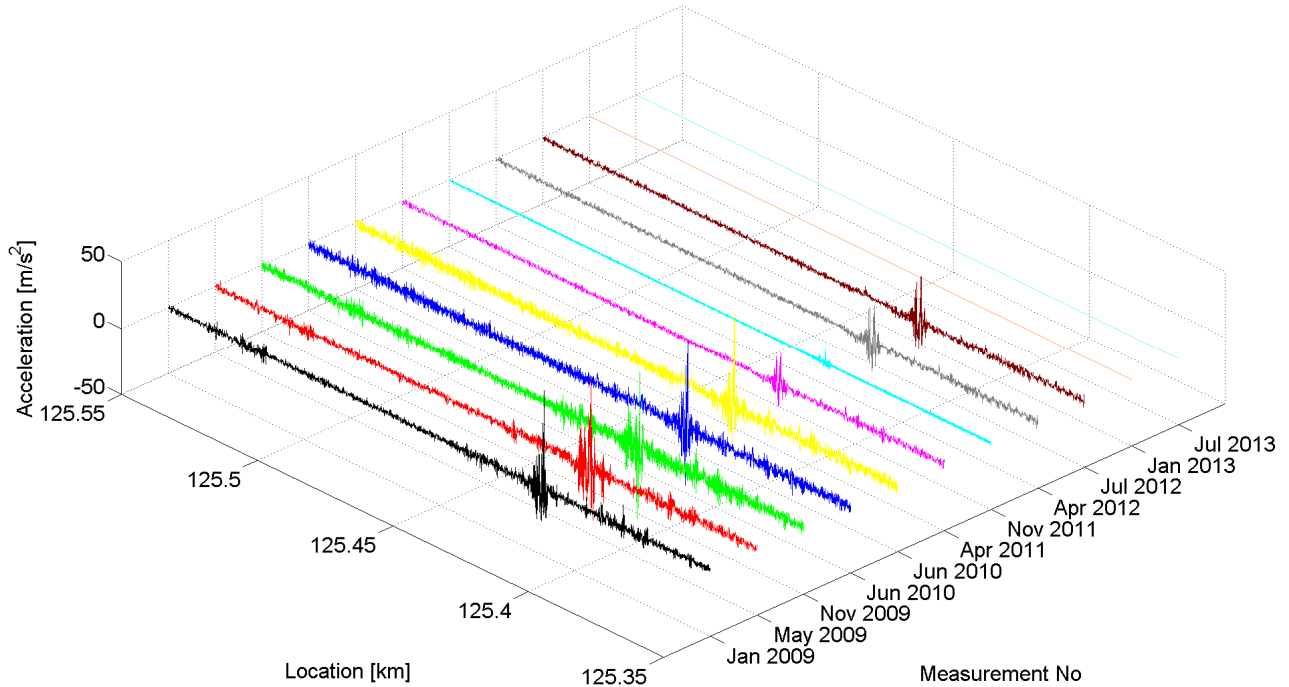


Figure 5.20: Wichtrach Turnout 9, lateral acceleration, axle box 1, right side

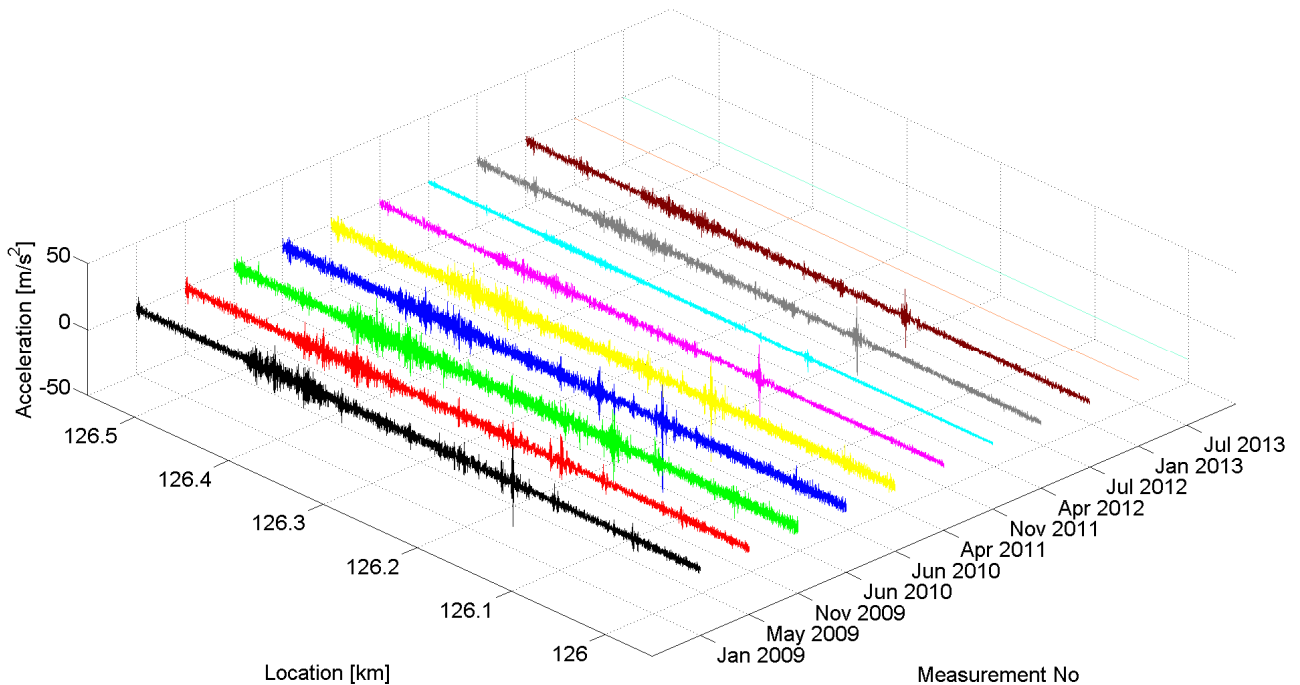


Figure 5.21: Wichtrach Turnout 20, lateral acceleration, axle box 1, right side

5.3 CONCLUSIONS

Axle box acceleration measurements were investigated to learn about the train-track interactions during a turnout crossing for different turnout types and turnout configurations (geometry, with/without USP, etc.).

Lateral acceleration levels on the left and on the right side but on the same axle showed differences by a factor of about 1.2 – 1.5. Differences in the lateral direction on the same axle were expected to be smaller and therefore, the difference between the two levels can be interpreted as an indicator for the measurement uncertainty for the set-up in use.

Rail grinding reduced the rms-values of the measured acceleration levels in vertical direction in the close vicinity of the turnout. However, the interaction of the turnout with the vehicle does not show any effect from rail grinding as expected. The impulse caused by the turnout is not significantly influenced by the combined wheel-rail roughness.

The maximum acceleration level in vertical direction does not show any influence of the under sleeper pads when compared to the same turnout geometry but without under sleeper pads. However, the rms-value before and after (close vicinity of) the crossing nose was smaller by a factor of about 2 for the track without under sleeper pads in comparison with the track with under sleeper pads.

For the comparison of different turnout designs the impulse energy was calculated for the zone of turnout-vehicle interaction. For the four turnouts in Rubigen the lowest impulse energies were calculated for Turnout 12. The results are in well agreement with the frog acceleration measurement results presented in [1]. Calculated impulse energies were lower for the turnouts in Wichtrach when compared to the levels calculated for the turnouts in Rubigen. In Wichtrach the turnout with a radius of 300 m resulted in higher impulse energies in comparison to the two turnouts with a radius of 900 m.

The impulse energy in vertical direction was larger by a factor of about 1.8 and 2.1 respectively in average for a turnout with a small radius of 300 m in comparison to a turnout with a radius of 900 m. In the lateral direction the acceleration levels are larger by a factor of about 2 for the turnout with a radius of 300 m when compared to the turnout with a radius of 900 m.

6. NUMERICAL SIMULATION FOR OPTIMIZING THE GEOMETRY OF CROSSING NOSE, IN TERMS OF GROUNDBORNE VIBRATION GENERATION

Impact load at the crossing nose has been identified as one of the major source of ground vibration generation in a turnout. One way of reduction is to propose a geometry optimization of the crossing part in order to reduce the impact load. The following chapter presents a numerical simulation that supports this optimization.

6.1 CROSSING GEOMETRY

A fixed railway crossing constitutes a kinematical challenge in terms of vehicle dynamics. The fact that two different rail and wheel paths intersect at one point requires that there exist flangeways which allow the wheel flanges to pass through the crossing. Therefore the rails are split into a crossing nose and two wing rails. The layout for a crossing panel with a fixed crossing and a photo of a crossing installed in track are shown in Figure 6.1.

When a wheel passes over the crossing in the facing move (from the switch panel towards the crossing panel) it will first encounter the wing rail. Due to the outwards deviation of the wing rail, the wheel/rail contact point will move towards the field side of the wheel profile. For a typical conical wheel profile, the rolling radius will decrease and the wheel will move downwards unless the wing rail is elevated. The reduced rolling radius on the crossing side will induce a yawing motion of the wheelset towards the crossing. Due to the check rail, the lateral motion of the wheelset is restrained and wheel flange interference contact with the crossing nose is prevented. When the wheel reaches and comes into contact with the crossing nose the contact load is quickly transferred from the wing rail to the crossing nose. For a typical conical wheel profile, the rolling radius increases as the new contact point is close to the flange root. The transition typically results in a significant impact force on the crossing nose as the slight downward motion of the wheel trajectory is reversed and the wheel is accelerated upwards by the crossing nose. This impact force induces airborne impact noise, ground-borne vibration and ground-borne noise.

In principle it is possible to design a crossing geometry that minimises the vertical variation in wheel trajectory and assures a smooth transition for a given wheel profile. The problem arises in tracks where a single crossing geometry encounters a variation of wheel profiles at different states of wear.

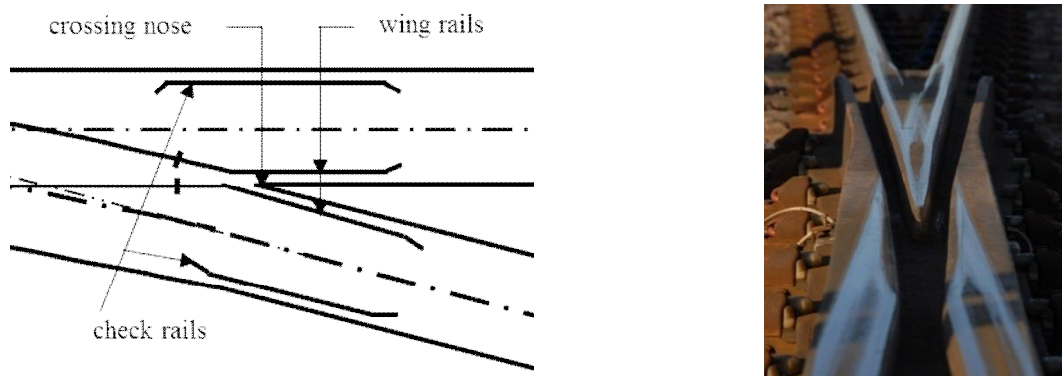


Figure 6.1. Principle sketch of a crossing panel (left), photo of a crossing in track (right)

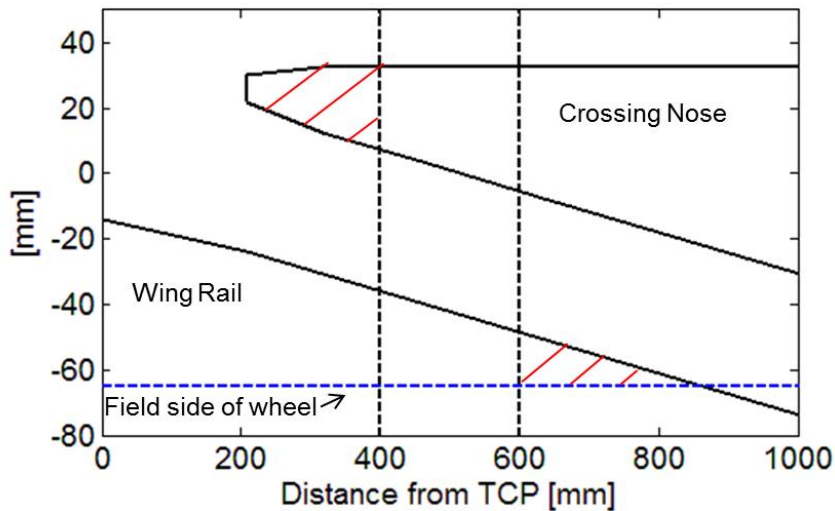


Figure 6.2. Top view of crossing geometry (TCP = theoretical crossing point)

Figure 6.2 shows a schematic top view of a fixed crossing. The vertical dashed lines indicate the beginning and end of the transition zone. The exact extension of the transition zone can vary, but it can be concluded that wheels should not make contact with the crossing nose where it is too thin to carry the full wheel load, and it should not make contact with the wing rail where the overlap between wheel and wing rail is too small to provide satisfying contact conditions. These parts are marked with red stripes in the figure. Thus, there is a given (short) distance where all wheels passing over the crossing have to make their transition from wing rail to crossing nose or from crossing nose to wing rail.

As there is a variation of wheel profile shapes in traffic and all of these profiles preferably should be able to experience an orderly transition from wing rail to crossing nose, the transition point for each wheel profile need to be within the transition zone. The transition point can be defined as the longitudinal location where a given wheel profile is in simultaneous contact with both the wing rail and crossing nose.

Figure 6.3(a) shows the contact situation for two wheel profiles at a given cross-section in the crossing panel. It can be seen that one wheel profile (blue) is in simultaneous contact with the wing rail and the crossing nose, while the other wheel profile (red) is only in contact with the wing rail. In this situation the first wheel profile is thus in the process of transition from wing rail to crossing nose while relative movement between the wing rail and the crossing nose would be required for the other wheel profile to also make contact with the crossing nose. Figure 6.3(b) shows the contact situation for the two wheel profiles at another cross-section further down the crossing. Here the second wheel profile is at its transition point, while the first wheel profile is only in contact with the crossing nose.

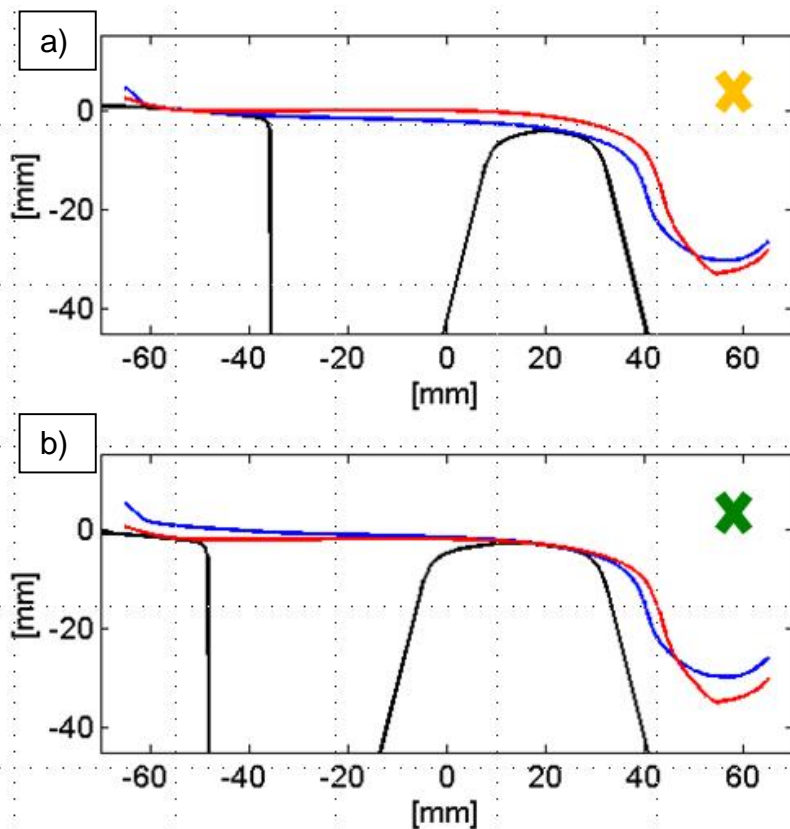


Figure 6.3: Wheel/rail contact for two different wheel profiles at two longitudinal positions in the crossing panel

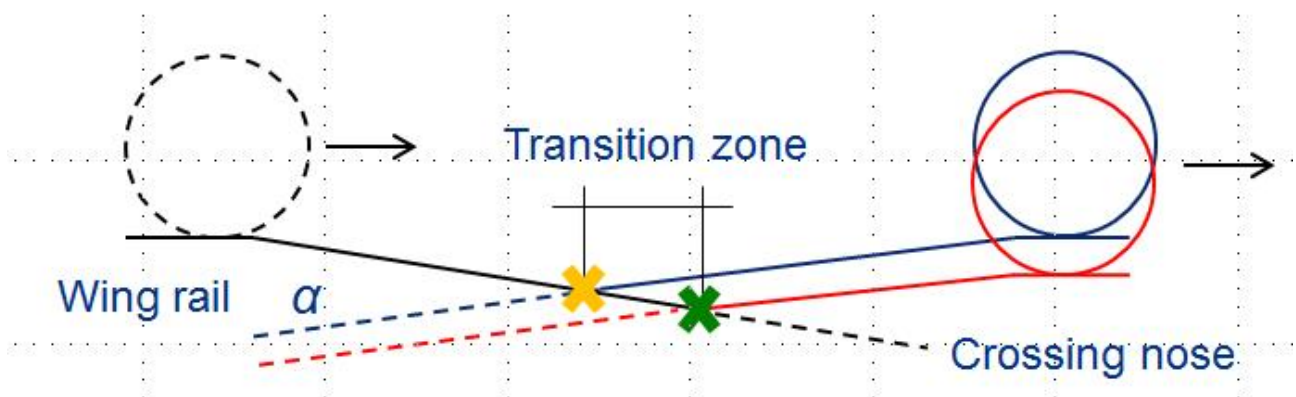


Figure 6.4: Wheel trajectories on wing rail, crossing nose for two different wheel profiles

The transition points for these two different wheel profiles therefore cannot be the same for reasonable rail profile geometries. This means the wheel trajectories on the wing rail and crossing nose have to move vertically relative to each other in the transition zone. Schematic vertical wheel trajectories of the two wheel profiles and their corresponding transition points are shown in Figure 6.4. The indication crosses (yellow and green) in Figure 6.3 and Figure 6.4 link cross-section to transition point.

The conclusion from this discussion is that a given transition zone length and a given spread in wheel profile geometry influences the necessary kink angle α (see Figure 6.4) of the crossing design as a certain amount of relative movement between wing rail and

crossing nose is needed to make sure that all wheel profiles reach the necessary contact conditions for transition within the zone. As the kink can cause significant vertical acceleration of the wheel, a crossing passage is typically associated with a significant impact force.

Starting from the above problem description, the focus of this investigation is to find the best crossing geometry compromise for a given spread in wheel profile geometry. The best compromise is the crossing geometry that minimizes the vertical wheel accelerations (and impact load inducing ground-borne vibration) and the contact pressures for the representative set of wheel profiles chosen for the evaluation. For this purpose, an optimization procedure is outlined below.

6.2 RAIL PROFILE PARAMETERISATION

The crossing geometry is parameterised on two levels using a current crossing design as a starting point. The cross-sectional rail profiles of the crossing nose and wing rail are parameterised as well as are the longitudinal height profiles of the crossing nose and wing rail. The cross-sectional and longitudinal height parameterisations are superimposed on each other. A change in profile height corresponds to a rigid body translation of the cross-sectional profile. All parameterised shapes are described using B-splines. For more details, see [6]. The selected base design is a 60E1-760-1:15 crossing, corresponding to a turnout with 60E1 rails, curve radius 760 m and crossing angle 1:15.

The shape of the longitudinal crossing nose profile is determined by two control points whose vertical movement is controlled by the design variables u_1 and u_2 . The shape of the longitudinal wing rail profile is similarly determined by the two design variables u_6 and u_7 . Both parameterisations are shown in Figure 6.5.

The two fixed control points at the upper end makes sure that the spline curve is tangent to the nominal profile as it enters the kink at about 1200 mm from the Theoretical Crossing Point (TCP).

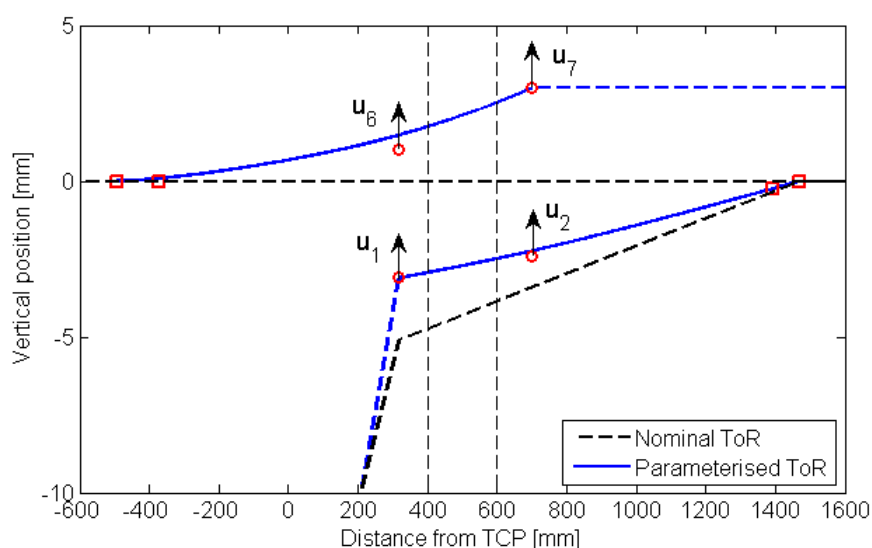


Figure 6.5: Parameterised shapes of the longitudinal height profile of the crossing nose and wing rail compared to the nominal configuration

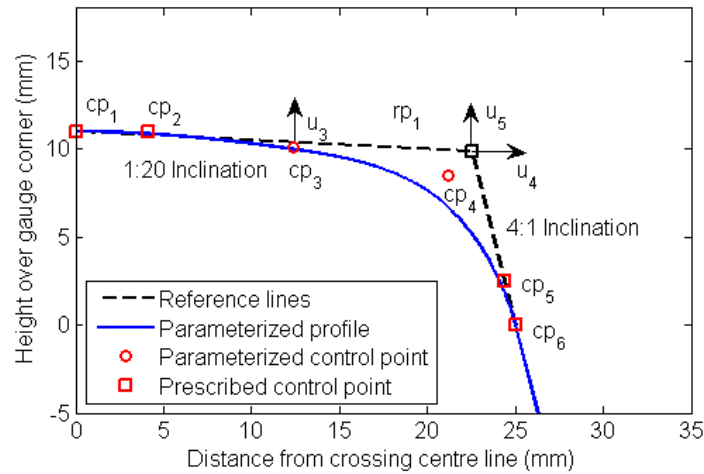


Figure 6.6: Parameterisation of the crossing nose profile

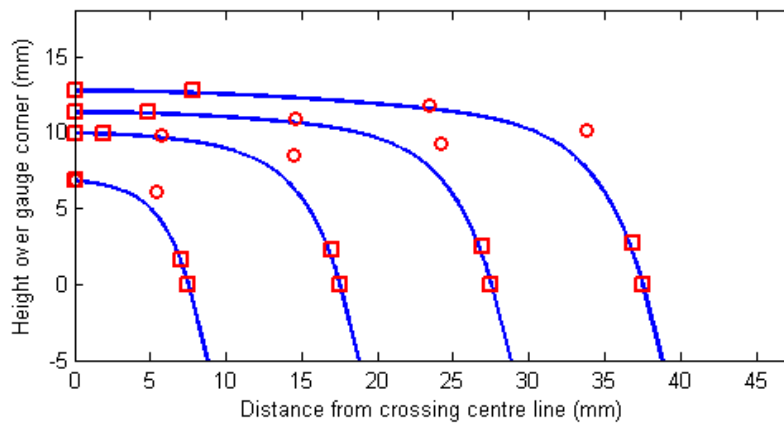


Figure 6.7: Semi cross-sections at four different thicknesses of the crossing nose

The parameterisation of the crossing nose profile is more complex as the rail cross-section changes significantly in the longitudinal direction. Three design variables u_3 , u_4 and u_5 are used, see Figure 6.6. The parameterisation is performed relative to a changing reference frame determined by the intersection of the two dashed reference lines. For more details about the parameterisation of the crossing nose profile, see [6]. In Figure 6.7, the parameterisation of the crossing nose profile is illustrated by the rail cross-section at four different thicknesses.

The wing rail cross-sectional profile is also parameterised using three design variables as illustrated in Figure 6.8. There are thus ten design variables in total.

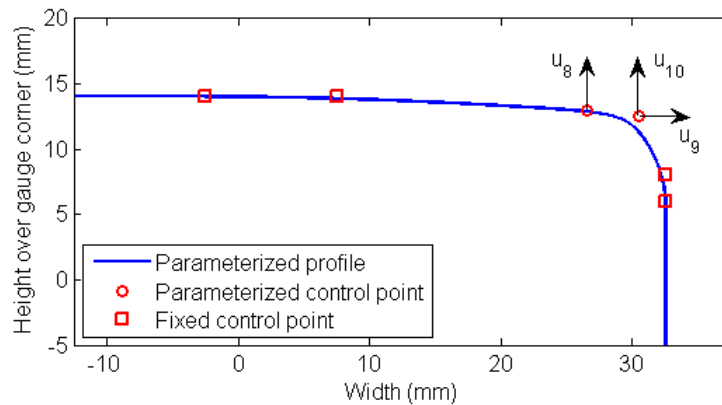


Figure 6.8: Parameterisation of the wing rail profile

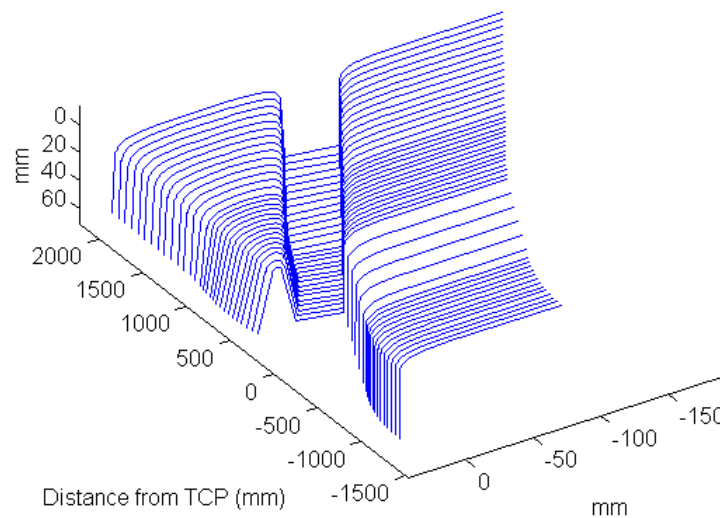


Figure 6.9: Parameterised crossing geometry

The resulting parameterised crossing geometry (with one wing rail excluded) is shown in Figure 6.9. The inter-profile spacing shown is the one used in this study. The inter-profile spacing is 50 mm in the transition zone.

6.3 OPTIMISATION PROCEDURE

The applied optimisation procedure can be summarised in the following points:

- Based on a database of 120 measured wheel profiles from Y25 bogies, a representative sample of five profiles is generated using Latin Hypercube Sampling. It is assumed that the measured set of wheel profiles corresponds to a representative range of freight wheels used in traffic.
- The feasible transition zone is defined.
- The optimization is based on two steps of quasi-static calculation:
 - Rail profile: the Hertzian contact pressures on the crossing nose and wing rail are evaluated using the GENSYS module KPF [7], and are minimised for a unit load by optimising the cross-sectional rail geometry.

- Longitudinal height profile: the vertical wheel acceleration during a crossing passage is minimized by optimizing the longitudinal height profiles.
- Seven lateral wheel positions are evaluated, $y_{lat} = [-3 -2 -1 0 1 2 3]$ mm
- The optimization is performed using Matlab's genetic algorithm *ga*

Examples of optimised rail cross-sections are shown in Figure 6.10 (crossing nose) and Figure 6.11 (wing rail). The optimization of rail cross-sections is discussed in more detail in [6]. However, as impact loads and the generation of ground-borne vibration are more determined by the wheel trajectories, in the following the focus is on the optimization of longitudinal height profiles.

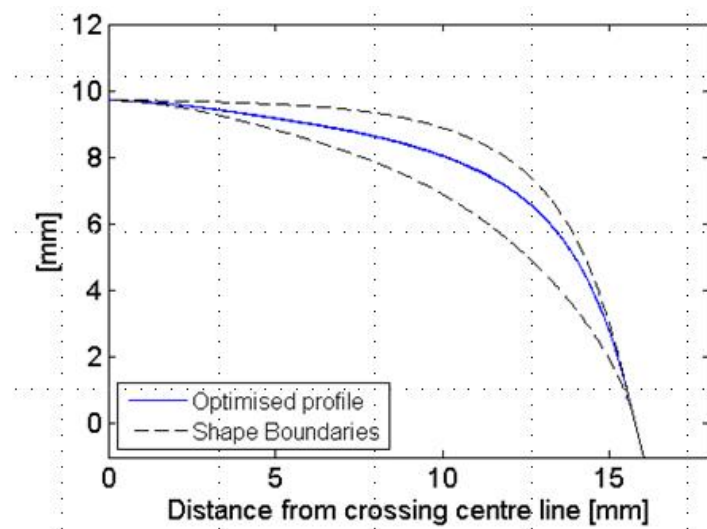


Figure 6.10: Example of optimised crossing nose profile and shape boundaries

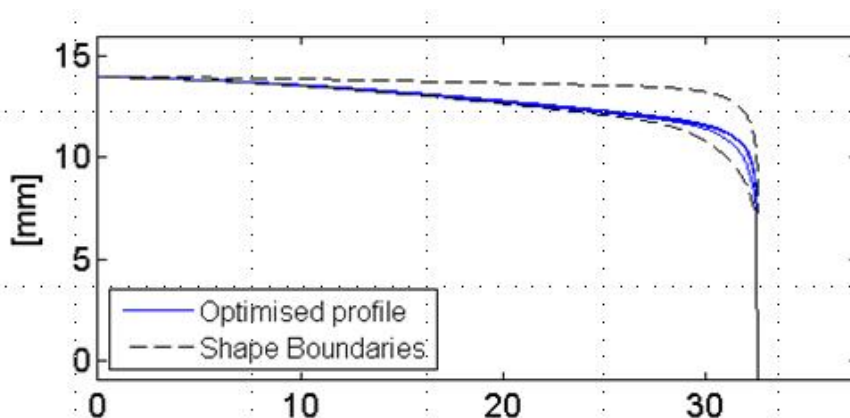


Figure 6.11: Example of optimised wing rail profile and shape boundaries

6.4 OPTIMISATION OF LONGITUDINAL PROFILES

In the optimization of the longitudinal height profiles, the optimised rail cross-sections from the previous optimization step are used. The feasible transition zone is here specified as 400 – 600 mm from the TCP.

The optimization objective is based on an estimate of the vertical wheel accelerations as the sample of wheel profiles passes over the crossing. In each iteration, the crossing de-

sign is realized as a function of the design variables u_1 , u_2 , u_6 , and u_7 that control the longitudinal height profiles (see Figure 6.5). Then the vertical wheel trajectory for each wheel profile is calculated for this crossing geometry. By fitting a polynomial to the wheel trajectory curves and differentiating twice, estimates of the vertical acceleration are obtained. A vector norm based objective is then calculated as a function of the acceleration estimate of all wheel profiles. A larger objective means larger accelerations and therefore larger impact forces. For details on the objective, see [6].

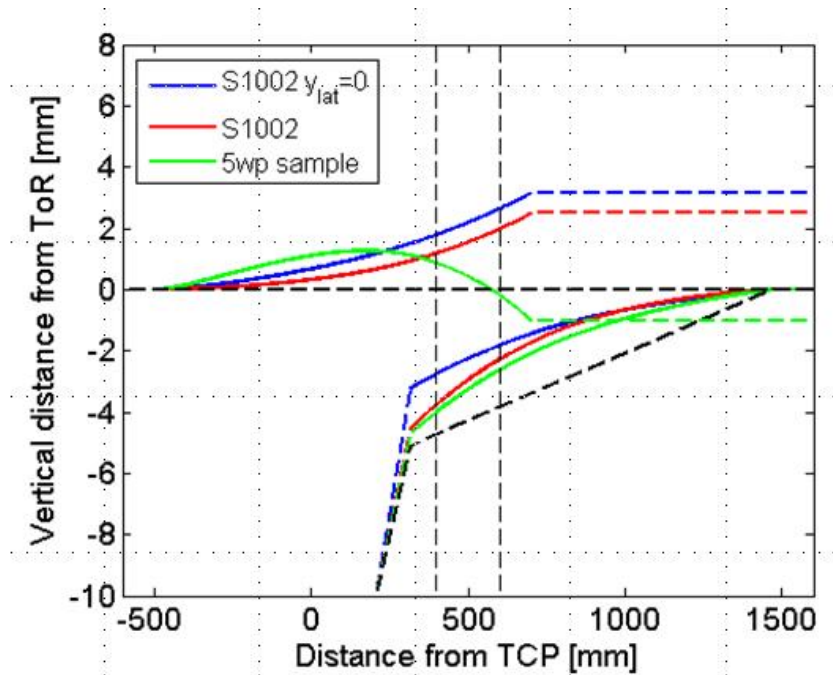


Figure 6.12: Optimised longitudinal profiles for different wheel profile configurations

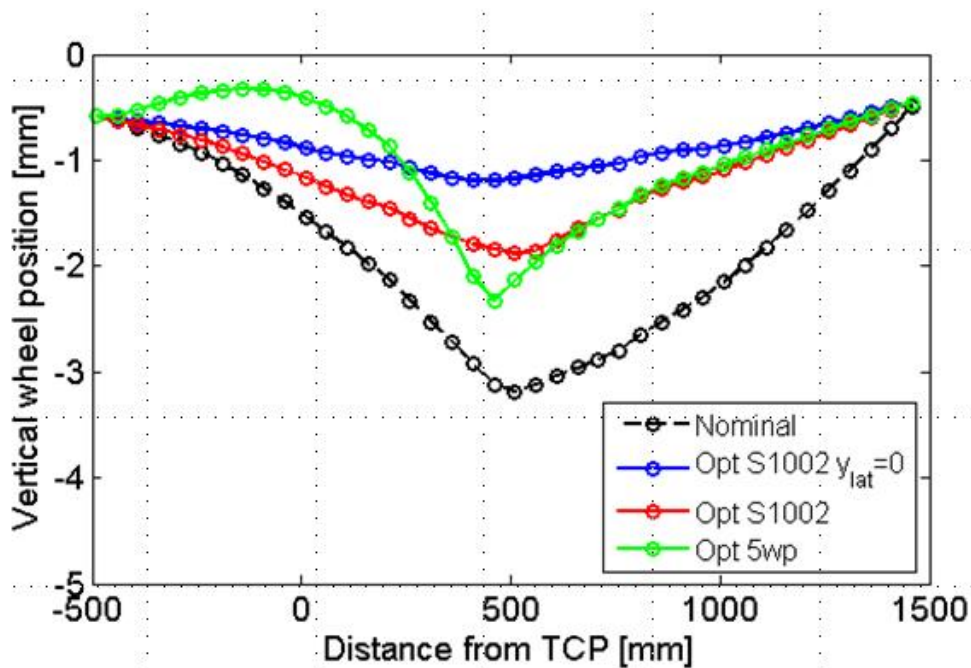


Figure 6.13: S1002 wheel profile on different optimised geometries

Figure 6.12 shows the optimised longitudinal height profiles for different levels of spread in wheel profile geometry: a single S1002 wheel profile at zero lateral displacement, a single S1002 wheel profile at all seven lateral displacements from -3 to 3 mm, and a wheel profile sample of five measured wheel profiles at all lateral displacements. To better illustrate the kink magnitudes associated with these longitudinal height profiles, the vertical wheel trajectories obtained for an S1002 wheel profile on the corresponding crossing geometries are presented in Figure 6.13. The figure also includes the vertical wheel trajectory for the nominal configuration without any alteration of the longitudinal height profiles.

As discussed in Section 6.1, the spread in wheel profile geometry constrains the feasible gradients of the wing rail and crossing nose. It is therefore not surprising to find that the S1002 profile at a single lateral displacement corresponds to the most shallow vertical wheel trajectory while an increasing spread in wheel profile geometry requires a larger kink magnitude.

The optimization routine maximizes the use of the feasible transition zone in that it finds the longitudinal height profiles that correspond to the smallest possible kink magnitude for a given transition zone and a given spread in wheel profile geometry. This is illustrated in Figure 6.14 which shows the vertical wheel trajectories for a S1002 wheel profile at all seven lateral displacements on the crossing geometry optimised for this spread in wheel profile geometry. It can be noted that the transition points (the lowest point for each trajectory) fills the transition zone between the two dashed vertical lines.

This can also be observed in Figure 6.15, which shows a histogram of the transition points for all calculated wheel profile trajectories in the optimization (5 wheel profiles and 7 lateral displacements = 35 trajectories) on the nominal and the optimised crossing geometry. For the optimised crossing geometry all transitions are within the defined transition zone, while the spread is larger for the nominal configuration.

The benefit of the optimised crossing geometry is that poor contact conditions are avoided and the maximum contact pressure for a passing wheel profile sample is reduced [6]. On the other hand, a larger kink magnitude is required to shorten the effective transition zone for the given wheel profile sample. It must therefore be stated that it is uncertain whether the optimised configuration would actually perform better in track.

The optimization is based on assumptions about the feasible transition zone. For future work it is desired to formulate an objective criterion that estimates the degradation rate of the crossing geometry (and perhaps the passing wheels) as a function of the wheel profile sample. This is however a criterion which is much more involved and difficult to estimate. Another alternative formulation is to optimize using a criterion that seeks a more uniform spread of the transition points within the transition zone as to spread the damaging impact forces within the transition zone.

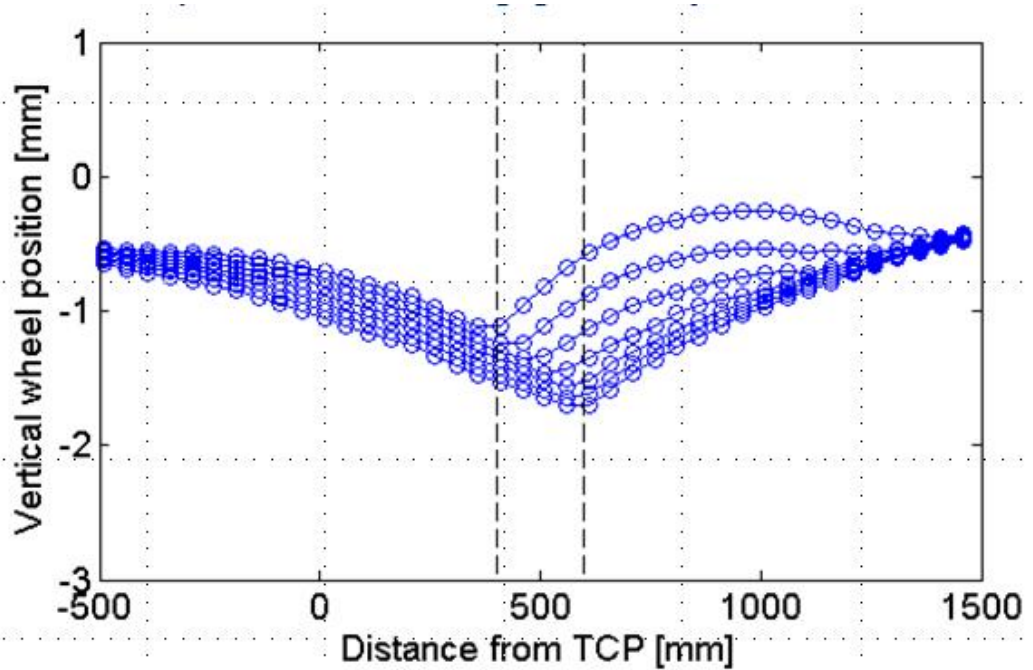


Figure 6.14: Seven vertical wheel trajectories for the S1002 profile on the corresponding optimised crossing geometry

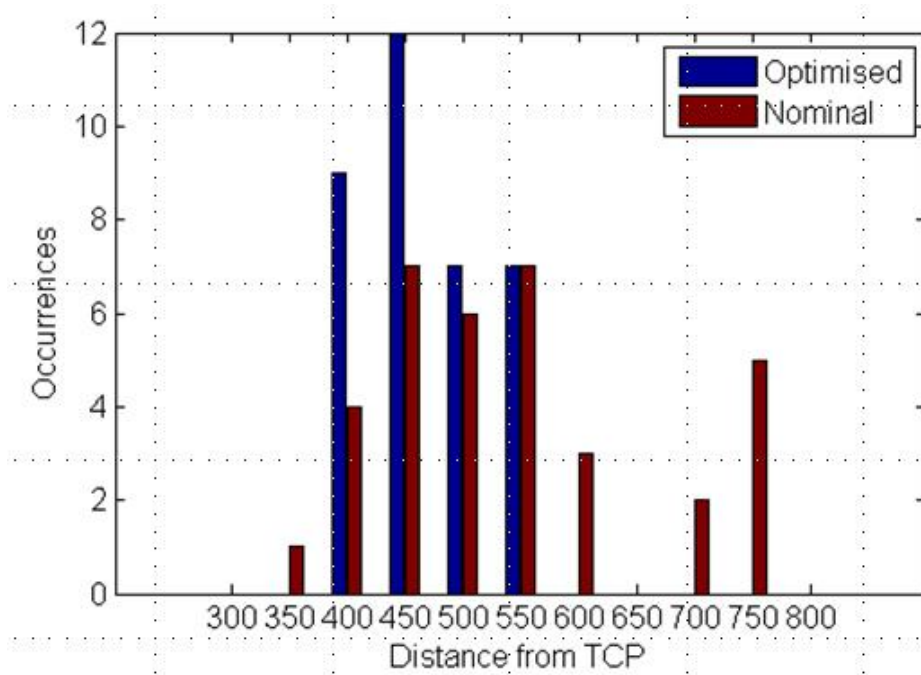


Figure 6.15. Histogram of transition points

In order to demonstrate that the optimization algorithm can find crossing geometries that in terms of wheel acceleration perform better than the nominal, additional optimizations are performed for different lengths of the transition zone. The zone lengths are 400 – 600 mm from the TCP as already investigated, and the extended zones 350 – 650 mm and 325 – 700 mm from the TCP.

The longitudinal height profile configurations found in these optimizations are shown in Figure 6.16, while the vertical wheel trajectories for a S1002 wheel profile at zero lateral displacement on these crossing designs are shown in Figure 6.17. It can be noted that a longer transition zone allows for a more shallow kink angle. The more shallow kink also corresponds to a smaller wheel acceleration objective. The acceleration objective values for the investigated zones and the nominal configuration are shown in Table 6.1. It can be noted that for the longest feasible transition zone an acceleration objective value is found which is lower than for the nominal geometry. The lower wheel acceleration is expected to result in a lower impact force and a reduction of induced ground-borne vibration.

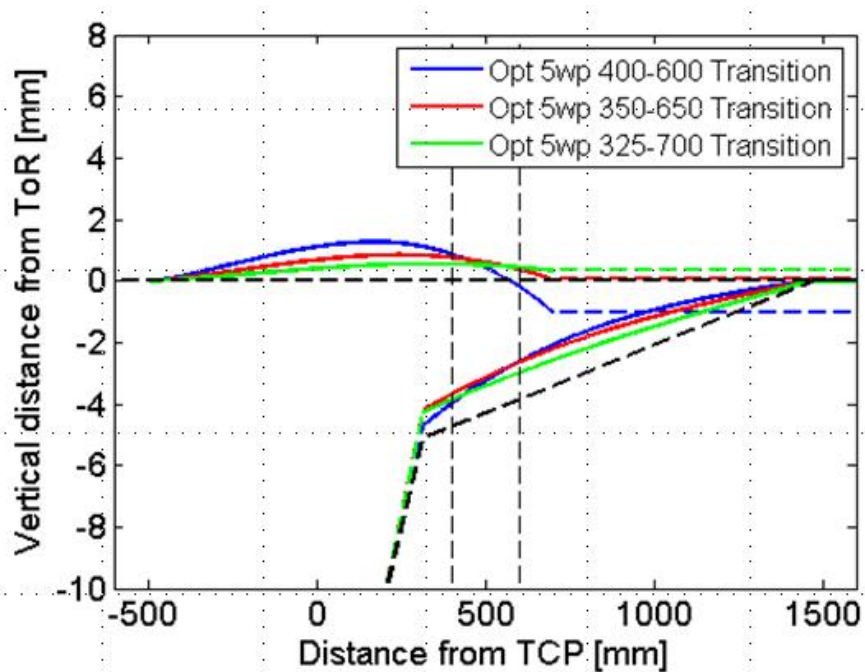


Figure 6.16: Influence of transition zone length on optimized longitudinal profile

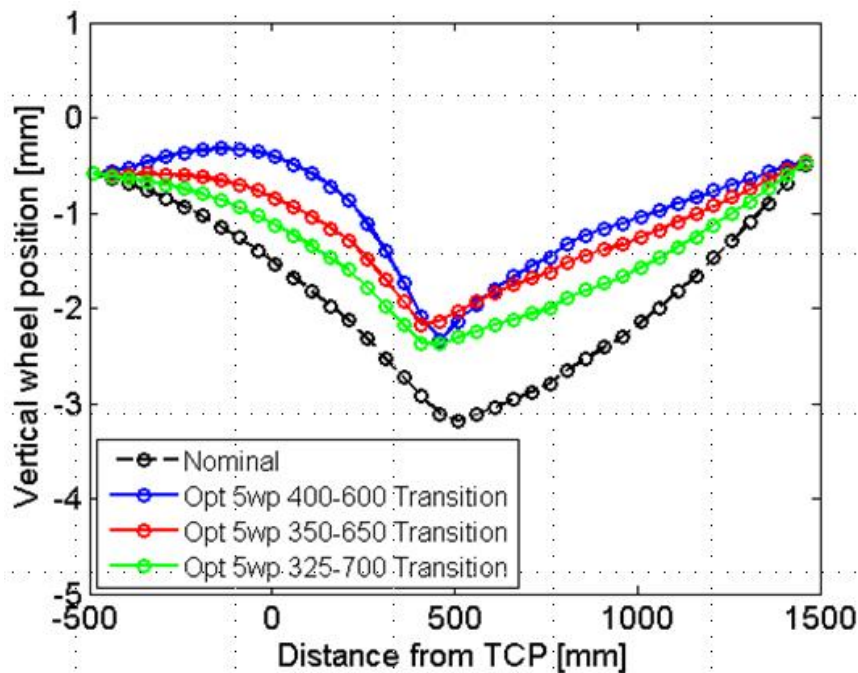


Figure 6.17: S1002 wheel profile on the optimised geometries in Figure 6.16

Table 6.1. Acceleration objective for a S1002 wheel profile (lateral wheel position 0 mm) on the optimised geometries in Figure 6.17

Run	Acc. Objective
Nominal	5.1e-3
Opt 5wp 400-600 Transition	8.4e-3
Opt 5wp 350-650 Transition	5.5e-3
Opt 5wp 325-700 Transition	4.6e-3

6.5 CONCLUSIONS

Measures to mitigate ground vibration induced by turnouts mainly aim at reducing the dynamic wheel/rail contact force (impact load) in the crossing panel of a turnout. A smooth wheel transition between wing rail and crossing nose is important to achieve low energy impacts on the crossing.

Measures to mitigate the vibrations include the use of soft or stiff Under Sleeper Pads (USP) for better and more stable turnout geometry over time. The use of USP may also reduce the magnitude of vibrations transferred from turnout to soil. Other measures include improving the design of the crossing panel (material and geometry of crossing nose and wing rails) and the use of more resilient rail pads.

According to this study, it seems difficult to design the rail profiles of the crossing panel such that it provides a smooth transition for a range of different vehicle types and speeds and for different wheel profiles (nominal and worn). A constraint that significantly limits the

potential for an optimised crossing design is the extent of the allowed transition zone where the wheels transfer from wing rail to crossing design and vice versa. The exact extension of the transition zone can vary, but it can be concluded that wheels should not make contact with the crossing nose where it is too thin to carry the full wheel load, and it should not make contact with the wing rail where the overlap between wheel and wing rail is too small to provide satisfying contact conditions.

The magnitude of the impact load is determined by the kink angle of the wheel trajectory where the wheel motion is reversed due to the transition between wing rail and crossing nose. To allow for a smaller kink angle in crossings, one could tighten the check rail tolerances (which determines the range of lateral wheel positions in the crossing) and set stricter tolerances on when wheel profile maintenance is required.

In RIVAS D3.6, the influences of vehicle speed, route and rail pad stiffness on the maximum impact load in the crossing panel were discussed. It was observed that a significant reduction in impact load at the crossing can be achieved by using softer rail pads. This seems to be a more realistic and robust design option to reduce ground-borne vibration induced by crossings.

7. CONCLUSIONS

Ground vibration in a turnout is a very particular issue because various phenomena generate these vibrations. Detailed conclusions can be found at the end of the Chapter 4, 5 and 6. A short summary follows:

Chapter 4 details a measurement process that allows quantifying and identifying these different sources. The measurement analysis highlights that among the main phenomena that generate noise and vibrations, there are the variation of track global stiffness due to variation of track equipment along the turnout and the jump at the crossing nose. The first phenomena causes an increase of wheel-rail interaction force the second an impact load at the crossing panel.

Increase of interaction force and impact load are characterized in the chapter 5 with on-board measurements consisting in axlebox acceleration assessment. It is observed that USP installation in turnout does not seem to imply a reduction of interaction force, and that design of the turnout has a big impact on it.

As impact load at the crossing panel is one of the major source of ground vibration generation, the last part of that report proposes a numerical procedure to optimize geometrically the crossing panel so that this impact load is minimized. However, the high constraints on the crossing panel geometry due to the limited allowable dimensions of the transition zone reduce the effectiveness of such optimization. After this investigations, it seems more relevant to reduce the stiffness of the crossing panel by softening the railpads or by implementing under sleeper pads. It will consequently decrease the impact load at the nose.

8. LITERATURE

- [1] RIVAS Deliverable D3.6: Description of the vibration generation mechanism of turn-outs and the development of cost effective mitigation measures. February 2013, 86 pp
- [2] B. Faure, E. Bongini, A. Renoncourt and A. Pouzet: Experimental characterization of the vibro-acoustic behaviour of a switch. Proceedings of the 11th International Workshop on Railway Noise (IWRN11), Uddevalla, Sweden, 2013.
- [3] A. Ekberg (guest editor): Special Issue on Innotrack – Innovative Track Systems. Proceedings of the Institution of Mechanical Engineers, Part F: Journal of Rail and Rapid Transit, 224, 2010.
- [4] E. Kassa and J.C.O. Nielsen: Dynamic interaction between train and railway turn-out: full-scale field test and validation of simulation models. *Vehicle System Dynamics* 46(1):521-534, 2008.
- [5] D.J. Thompson: *Railway Noise and Vibration. Mechanisms, Modelling and Means of Control*, Oxford, Elsevier Science, 506pp, 2009.
- [6] B. Pålsson, Optimisation of railway crossing geometry considering a set of representative wheel profiles, Proceedings IAVSD2013, Qingdao, China, August 19-23, 2013, 10 pp
- [7] GENSY, www.gensys.se